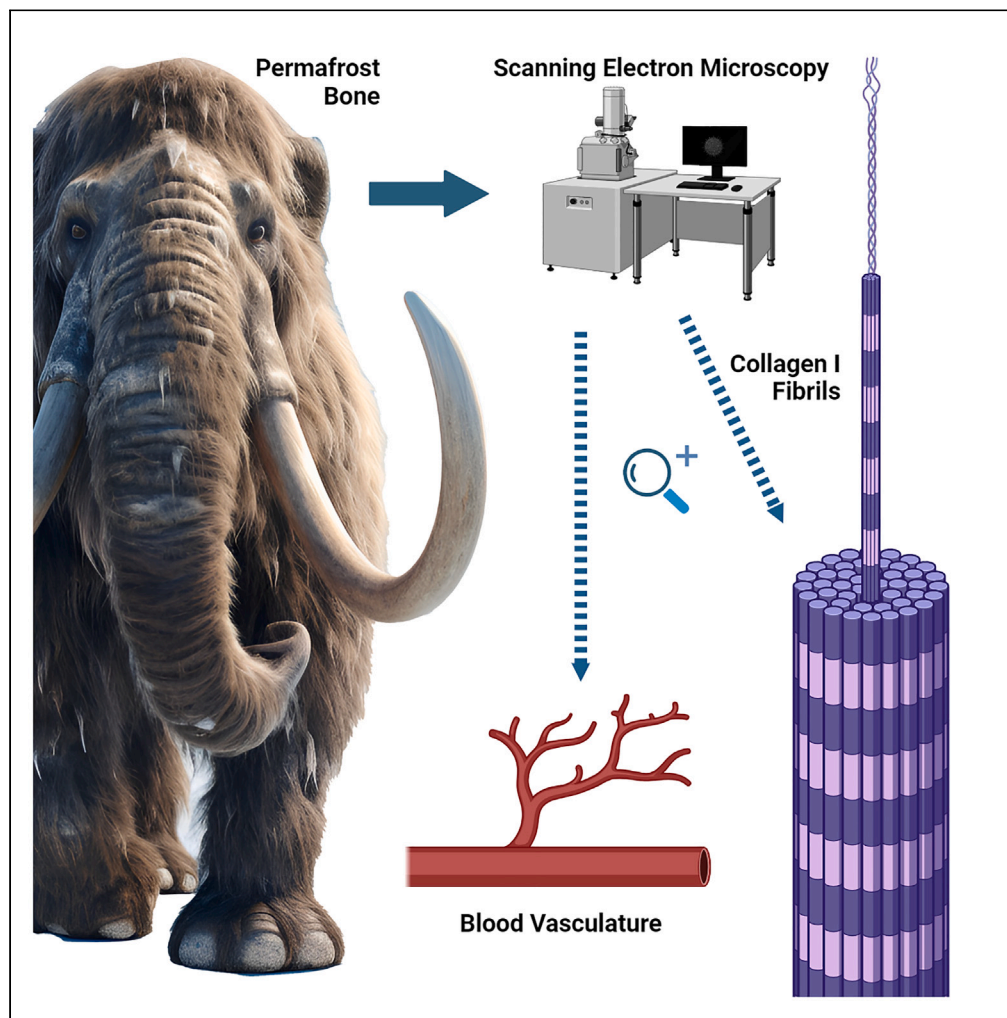**Article**

Nanoscopic imaging of ancient protein and vasculature offers insight into soft tissue and biomolecule fossilization

Landon A. Anderson

laander2@ncsu.edu

Highlights

First extensive nanoscopic, 3D imaging of ancient collagen protein and vasculature

Imaged permafrost bones are subfossils preserving an underlying collagen framework

Fine-scale soft tissue diagenesis can be directly imaged across the geologic record

Nanoscopic approach is a potential proxy for ancient DNA/protein sequence recovery

Article

Nanoscopic imaging of ancient protein and vasculature offers insight into soft tissue and biomolecule fossilization

Landon A. Anderson[1,2,*]

SUMMARY

Fossil bones have been studied by paleontologists for centuries. Despite this, empirical knowledge regarding the progression of biomolecular (soft) tissue diagenesis within ancient bone is limited; this is particularly the case for specimens spanning Pleistocene directly into pre-Ice Age strata. A nanoscopic approach is reported herein that facilitates direct imaging, and thus empirical observation, of soft tissue preservation state. Presented data include the first extensive nanoscopic (up to 150,000× magnification), three-dimensional (3D) images of ancient bone protein and vasculature; chemical signals consistent with collagen protein and membrane lipids, respectively, are also localized to these structures. These findings support the analyzed permafrost bones are not fully fossilized but rather represent subfossil bone tissue as they preserve an underlying collagen framework. Extension of these methods to specimens spanning the geologic record will help reveal changes biomolecular tissues undergo during fossilization and is a potential proxy approach for screening specimen suitability for molecular sequencing.

INTRODUCTION

A sizable body of evidence suggests that biological "soft" tissues can preserve during fossilization, even into the early Neogene, Paleogene, and Mesozoic. Organisms trapped within fossil resins, for example, are renowned for their life-like preservation,[1] and ancient remains of pigmented skin,[2,3] blubber,[3] cuticular and chitinous coverings,[4,5] and internal organs[3,6] have all been reported. Even specimens preserving only biomineralized remains, such as bones and/or teeth, are reported to preserve osseous soft tissues including collagenous fibers, cells, and vascular tissue.[7–10]

While pre-Pleistocene specimens can preserve soft tissues and cells, relatively little is known regarding how the chemical processes responsible for this phenomenon progress.[11,12] Presumably, the soft tissues of most organismal remains are eventually degraded during fossilization, preserving only the mineral portions.[13–20] Soft tissues that avoid degradation undergo chemical transformation toward a more recalcitrant state.[11,21] For example, soft tissues of specimens as recent as the Pliocene generally exhibit extensive in-situ polymerization and/or carbonization.[22–24] Additionally, degree of ancient DNA and protein sequence recovery exhibits substantial drop-offs for strata dated prior to ~0.13–0.24 Ma[25] and ~0.8–1.0 Ma,[26–28] respectively. Combined, this suggests diagenetic reactions progress significantly within soft tissue specimens as the late/mid-Pleistocene transitions into the early Pleistocene/Pliocene. By the Pliocene, the biomolecules of most soft tissues would either be chemically transformed into organic, diagenetic macromolecules,[11,21–24,29] or degraded and potentially replaced with recrystallized mineral.[13–20] However, empirical observations of the progression of these diagenetic changes in soft tissue specimens spanning the Pleistocene into the Pliocene have generally, to this point, been scarcely reported.[11,12,30] This gap in knowledge is significant, as an empirical understanding of the changes biological tissues undergo during fossilization is linked to predicting a specimen's potential for harboring sequence-able DNA and proteins.[30]

Empirical analysis of bone biomolecular histology has recently been proposed for addressing the aforementioned stated gap in understanding regarding the progression of cell and tissue fossilization. Biomolecular histology refers to histological structure that is the direct manifestation of constituent biomolecules[30] (see Table 1 for a list of terms as defined within this paper). Cellular membranes, which are composed primarily of phospholipids along with various associated proteins and sterols,[31] are one example of biomolecular histology. Another would be the banded fibrils of the collagenous framework of bone; these banded fibrils are the direct, structural manifestation of collagen I sequences.[32,33] Biogenic minerals, including the bioapatite of bone, are strictly excluded from this definition. A biomolecular histological approach would thus report how the morphology and chemistry of such structures compare for specimens spanning the geologic record. Bone specifically is suggested as a model tissue because its non-mineral portion (defined herein as organic bone matrix [OBM], see Table 1) consists overwhelmingly (>90%) of a single biomolecule, collagen I protein.[32–34] This simplifies comparisons of ancient OBM against

[1]Department of Biology, North Carolina State University, Raleigh, NC, USA
[2]Lead contact
*Correspondence: laander2@ncsu.edu
https://doi.org/10.1016/j.isci.2024.110538

Table 1. Definitions list

| Term	Definition
Biomolecular histology	Histological structure that is the direct manifestation of constituent biomolecules; specifically excludes biogenic mineral portions, such as the bioapatite of bone[30,39]
Biomolecular tissue; soft tissue	The non-mineral portion of tissues; a specific example would be organic bone matrix (OBM)
Bone; bone tissue	A highly mineralized collagen I framework of biological origin; includes various associated non-collagenous proteins and cellular portions such as vascular tissue, osteocytes, nervous tissue, etc.[32–34]
Collagen I framework; collagenous framework	The underlying, central structure of bone onto which bioapatite mineral is deposited; consists of intertwined bundles collagen I protein fibrils and potentially some minor non-collagenous portions[32–34]
Fossilization	A process or series of processes involving substantial physical *and* chemical alteration of a specimen from its original state, which ultimately facilitate its preservation within the geologic record[19,20,40,41]; within context of this definition, a substantial yet transient physical alteration alone, such as burial followed by freezing, is not sufficient in-and-of-itself to be considered fossilization
Fossil bone; fossil bone tissue	Remains of original bone tissue preserved within the geologic record that, at most, preserve only a marginal degree of the original OBM (non-mineral portion); *within this manuscript, a "marginal degree of the original OBM" is defined as the absence of an underlying collagen I framework*; please see Methods S1 of the Supplemental Information for supporting references
Organic bone matrix (OBM); osseous soft tissues	The non-mineral portion of bone; includes the collagen I framework and associated non-collagenous proteins and cellular portions such as vasculature, osteocytes, nerve cells, etc.[11,32–34]
Subfossil bone; subfossil bone tissue	Remains of original bone tissue preserved within the geologic record that preserve a substantial degree of the original OBM (non-mineral portion); *within this manuscript, a "substantial degree of the original OBM" is defined as the presence of an underlying collagen I framework*; please see Methods S1 of the supplemental information for supporting references

Regarding the terms "fossil bone" and "subfossil bone," please see the commentary given in Methods S1 of the supplemental information for background regarding the definitions chosen for these terms within this manuscript.

modern-day collagen controls and standards. Furthermore, ancient bone specimens are often more accessible for molecular analyses relative to rarer, non-biomineralized remains, and soft tissues have been readily reported to preserve within ancient bone specimens from a variety of sedimentary contexts.[7,9,10,29,35–38]

A pilot study is presented here that demonstrates a nanoscopic approach to empirically studying the changes OBM biomolecular histology undergoes during fossilization. This will provide an initial dataset for comparing the preserved state of OBM (at the biomolecular histological level) for specimens spanning the late/mid-Pleistocene into the Pliocene/Miocene. Permafrost bones are specifically chosen for this initial investigation because they are well studied regarding gross biochemical preservation. Genomic studies of permafrost bone extracts,[42–45] as well as some proteomic[42,46,47] and isotopic investigations,[48–50] have reported excellent biochemical preservation. DNA fragments and a diversity of proteins are generally reported.[25,42,46] Sequence coverage for collagen I[42,46,47] is often comparable to that of extant bone.[51,52] This may suggest the original OBM of many permafrost bones is largely intact and not fully fossilized, and that the permafrost bones themselves consist of subfossil bone tissue (see Table 1 definitions for "fossilization" and "subfossil bone tissue"). However, testing such a hypothesis involves direct structural and chemical observation of the underlying OBM biomolecular histology. Direct structural and chemical observation of underlying biomolecular histology is sparsely documented for most Pleistocene specimens,[30] excluding the exceptional cases of frozen Pleistocene "mummies".[53–56] A few studies have reported images for OBM of latest Pleistocene bones using transmission electron microscopy (TEM) showing two-dimensional sections of collagen fibril banding.[57–60] A recent study even reported nanoscale, three-dimensional (3D) imaging of microstructures within the bones of Silurian and Devonian fish; however, the reported images were of empty osteocyte lacunae lacking any original biomolecular tissue.[61]

This study is the first to present extensive nanoscale (up to 150,000× magnification) imaging data characterizing the 3D structure and organization of collagen I protein fibrils and vasculature for *any* ancient bone (two preliminary images of ancient collagen at 50,000× mag. were presented in Anderson (2022)[30]). Time-of-flight secondary ionization mass spectrometry (ToF-SIMS) is also used to directly investigate the preserved chemical state of these structures. This is significant because such chemical data are localized to the specimen's biomolecular histological structure itself (as shown in the presented scanning electron microscope [SEM] images) with microscale resolution.[62] Past studies
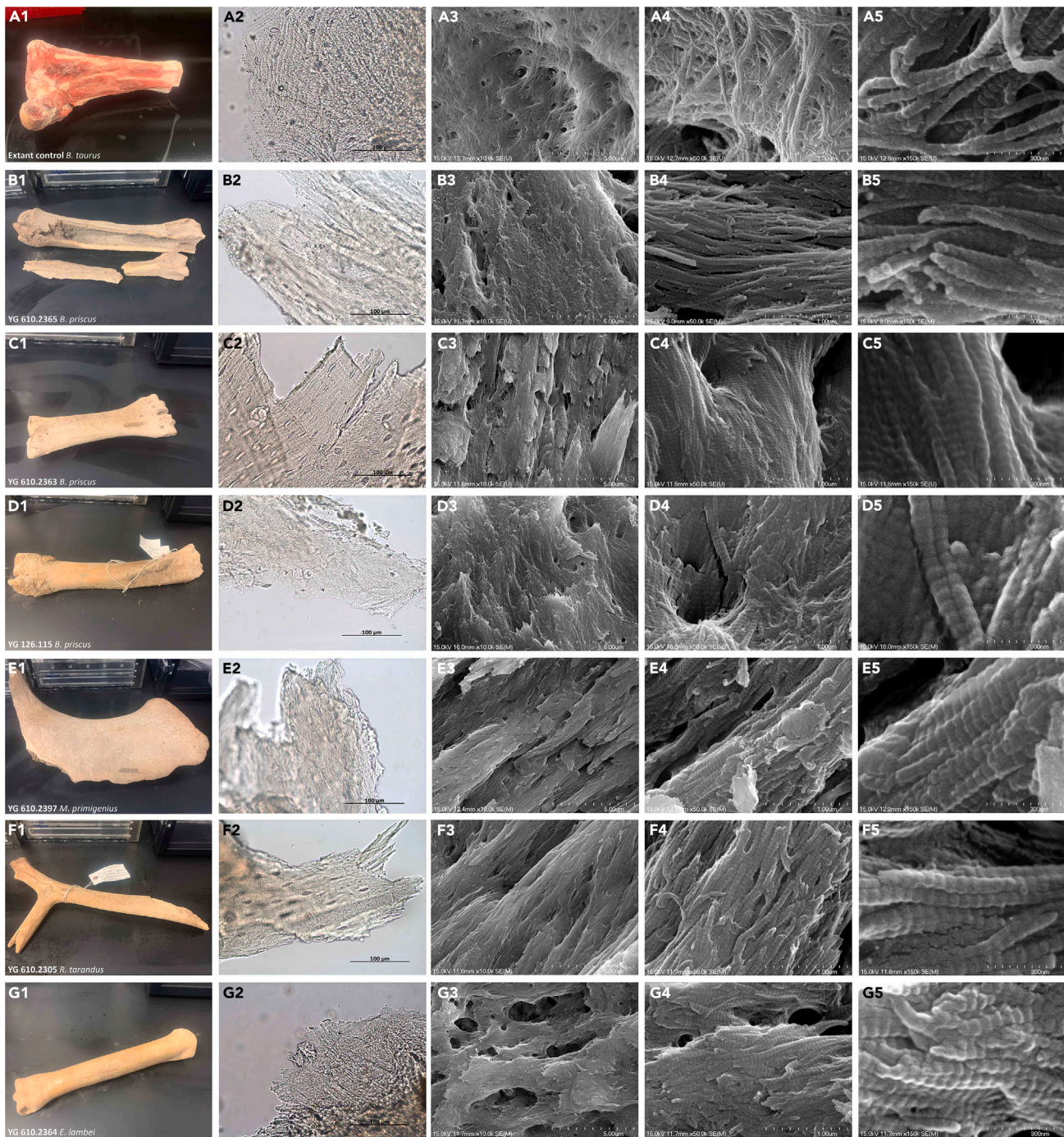
Figure 1. Hierarchical images of permafrost and extant organic bone matrix (OBM)

First shown are macroscopic images of the mineralized bone specimens (A1–G1). Then, transmitted light microscope imaging depicts the microscale, fibrous structure of demineralized OBM sections taken from the bone specimens (A2–G2). Lastly, scanning electron microscope (SEM) images of increasing magnification reveal how the fibrous structure shown by the transmitted light images is formed of nanoscopic collagen I fibrils (A3–G5).

(A1–A5) Extant *Bos taurus* long-bone.

(B1–B5) YG 610.2365 (*Bison priscus* radius).

(C1–C5) YG 610.2363 (*Bison priscus* metatarsal).

(D1–D5) YG 126.115 (*Bison priscus* tibia). Desiccated soft tissue can be observed on the exterior surface of this specimen.

Figure 1. Continued
(E1–E5) YG 610.2397 (*Mammuthus primigenius* innominate).
(F1–F5) YG 610.2305 (*Rangifer tarandus* antler).
(G1–G5) YG 610.2364 (*Equus lambei* metatarsal).

have instead generally used homogenized extracts that preclude localizing chemical signal to tissue structure.[30] Finally, carbon:nitrogen (C:N) ratios are reported for the various specimens herein to allow for direct comparison against previous studies of permafrost bone.[48–50]

These analyses test the hypothesis that the biomolecular histological preservation of collagen fibers and vascular tissue for permafrost bone is consistent with prior genomic, proteomic, and isotopic data; that is, these permafrost specimens are not fully fossilized but instead represent subfossil bone tissue. The methodology used by this study thus allows for direct observation and evaluation of OBM preservation state, to the point that fossil and subfossil bone tissue can be readily identified and distinguished in a *non-arbitrary* manner. If a sample of ancient bone tissue is observed to possess a collagen I framework (as can be confirmed by direct imaging of collagen I fibrils, such as with the data presented by this paper), then that bone tissue would be considered subfossil bone tissue. If, alternatively, a sample of ancient bone tissue is observed to lack a collagen I framework, then that bone tissue would be considered fossil bone tissue.

Such an approach can be readily extended to ancient bones from temperate and subtropical thermal settings, as well as earlier geologic timepoints. Doing so will help elucidate the fine-scale changes OBM, and biomolecular tissues in general, undergo during diagenesis. Ultimately, such fine-scale changes experienced by specimen OBM during diagenesis can be correlated with the degree to which a specimen preserves ancient DNA and protein sequences. Thus data generated by this study's direct imaging approach has potential to function as a proxy for screening ancient bone (among other specimen types) for degree of molecular sequence preservation. Anderson 2022 gives a more in-depth discussion regarding this potential application of the present study's methodology.[30]

RESULTS AND DISCUSSION

Permafrost specimens and elemental/isotopic analysis

The Pleistocene permafrost specimens comprise six bones recovered from the Little Blanche Creek and Irish Gulch localities of the Yukon Canadian territory (Figures 1B1–G1). The bones were each recovered as isolated, disarticulate remains which is typical for many Pleistocene specimens from eastern Beringia.[63,64] Notably, the *Bison priscus* tibia from Irish Gulch preserved remnant soft tissue (potentially ligaments and tendons, or even remnant musculature) still attached to the bone's external surface. The Beringian permafrost specimens were overall more brittle than the extant controls (Figures 1A1, S1A, and S1F), and external bone portions were generally discolored and somewhat friable. Care was taken to sample only the internal cortical bone layers that displayed minimal discoloration and brittleness. Post-demineralization, extant control OBM was stiff and rubber-like, and sterile razor blades were necessary to cut smaller sections. In comparison, the demineralized permafrost specimen OBM readily frayed into smaller fibers and was soft and pliable.

Stable isotope and C:N measurements obtained from demineralized bone samples are shown in Table 2. Both the permafrost and extant specimen C:N ratios were within the range 2.9–3.6, which has historically been accepted as indicating well-preserved collagen. Values for %C and %N (by mass) ranged from 41.0–46.0% and 15.2–17.1%, respectively, which is likewise consistent with the collagenous framework having undergone minimal diagenesis.[48–50,65] Measurements of $\delta^{13}C$ and $\delta^{15}N$ are also reported; while the obtained values are consistent with prior values obtained from permafrost megafaunal bones, they are more so related to organismal diet/trophic-level and thus are not further discussed.[48–50]

Collagen I protein fibers

Demineralized OBM sections exhibited an overall fibrous structure when visualized with transmitted light microscopy (Figures 1A2–G2; Figures S1B and S1G). Higher magnification images (Figures 1A3–G5; Figures S1C–S1E and S1H–S1J) confirmed this fibrous structure to be the result of collagen fibers, themselves consisting of collagen I fibril bundles. For extant bone collagen, these individual fibrils consist of parallel-packed chains of peptide helices (each helix consists of two α1 peptides and a single α2 peptide, intertwined). The peptide helices are bound one-to-another near their termini via covalent crosslinks; these chains are packed parallel to each other down the length of the fibril and with small longitudinal offsets that result in alternating regions of tightly/loosely packed peptides (see Figures 1 and 4 of Minary-Jolandan and Yu 2009[66]; Figure 3 of Orgel et al., 2006[67]). These alternating regions of density result in the ~67 nm banding pattern characteristic of extant collagen I fibrils.[32,33,66–68] Such a pattern is clearly present throughout the high magnification images of both the permafrost and extant OBM. The presence of this banding in the permafrost specimens indicates the collagen fibrils are, to an extent, well preserved. Chemical degradation has not occurred to substantially disrupt the packed structure of the peptide helices within an individual fibril.[68] The arrangement of the fibrils themselves with respect to one another does, however, potentially indicate some degree of chemical degradation. The fibrils of the Pleistocene specimens potentially display a somewhat "looser" association with one another relative to those of the extant controls, which are tightly intertwined. This suggests that the intermolecular forces holding the bundled fibrils together have been disrupted somewhat, perhaps due to chemical degradation of the constituent amino acids.[42,46] This would also explain why, post-acid demineralization, the OBM of the permafrost samples tended to easily fray in comparison to the stiffer, rubber-like matrix of the extant controls.

ToF-SIMS spectra collected for both permafrost and extant collagen fibers displayed high intensities for secondary ions characteristic of proteins[69–71] (Figures 2 and 3; Figures S4–S16). The distribution and intensities of their secondary ions closely mirrored the collagen I standard spectra. Relative to the hemoglobin and BSA standards, yields for $C_4H_6N^+$ (68.05 m/z), $C_4H_8N^+$ (70.07 m/z), and $C_4H_8NO^+$ (86.06 m/z)

Table 2. Stable isotope and C:N measurements

Specimen number	Sample	C:N (atomic)	%C (by mass)	%N (by mass)	$\delta^{13}C$ (‰) VPDB	$\delta^{15}N$ (‰) AIR
N/A	*Bos taurus* long-bone	3.1	41.0	15.3	−20.39	4.96
N/A	*Alligator mississippiensis* long-bone	3.0	44.6	17.1	−17.45	8.75
N/A	*Struthio camelus* long-bone	3.4	44.1	15.3	−20.31	4.93
YG 126.115	*Bison priscus* tibia	3.3	46.0	16.2	−19.76	6.46
YG 610.2305	*Rangifer tarandus* antler	3.1	44.4	16.7	−17.19	2.00
YG 610.2363	*Bison priscus* metatarsal	3.1	45.2	16.8	−19.84	5.53
YG 610.2364	*Equus lambei* metatarsal	3.1	44.2	16.4	−19.77	5.03
YG 610.2365	*Bison priscus* radius	3.1	41.8	15.6	−19.09	4.22
YG 610.2397	*Mammuthus primigenius* innominate	3.2	41.0	15.2	−20.38	7.21

secondary fragment ions were particularly high; in SIMS protein analyses, $C_4H_6N^+$ and $C_4H_8N^+$ are generally produced by the amino acid proline[69–71] ($C_4H_8N^+$ also corresponds to arginine,[71] which is somewhat common in collagen I[72–74]), and $C_4H_8NO^+$ by hydroxyproline[75] (see Figure 3 for the hydroxyproline-related ion peak); both amino acids are enriched within the collagen I sequence. Additionally, glycine makes up approximately one-third of collagen I.[72–75] The CH_4N^+ (30.04 m/z) ion formed by SIMS fragmentation of glycine is present in high abundances for the permafrost and extant OBM. However, this ion is ubiquitous to most amino acids and generally shows limited variation between spectra of different proteins, as was observed in this study.[69–71] These three amino acids are the most abundant within collagen I and are integral to forming the tight turns of its helical peptides.[66,67,72,76] The substantial presence of these ions, as well as overall spectral agreement with the purified collagen I standard, evidences the permafrost bone collagen framework is relatively well preserved. The BSA and hemoglobin spectra also exhibit elevated intensities for $C_4H_{10}N^+$ and $C_5H_{10}N^+$ relative to the collagenous spectra. These ions are typically produced by valine and lysine/leucine,[69–71] respectively, which are less prevalent in the collagen I sequence relative to BSA and hemoglobin[72–74]; for a list of secondary ions specifically examined within this study, along with potential source molecules, please see Table S1 and Table S2 within the supplemental information.

Peak areas for 27 amino acid-related ions[69–71,75] (Table S1) were calculated for each protein spectrum, placed in a data matrix, and analyzed with principal component analysis (PCA) (Figure 4). PC1 scores (56.5% explained variation) for the collagenous sample spectra were generally more positive, and PC2 scores (23.2% explained variation) were generally closer to zero. Loading values for $C_4H_8N^+$ and $C_4H_8NO^+$ show a substantial positive correlation with scores for PC1, supporting a relatively high abundance of proline and hydroxyproline within the collagenous sample spectra. Additionally, several secondary ions, including those corresponding to valine ($C_4H_{10}N^+$, 72.09 m/z) and lysine/leucine ($C_5H_{10}N^+$, 84.08 m/z), correlate negatively with PC1 scores. This was also the case for $C_4H_5N_2^+$ (81.04 m/z), $C_4H_6N_2^+$ (82.06 m/z), and $C_5H_8N_3^+$ (110.08 m/z), all of which correspond to histidine.[69–71] This agrees with the collagen I sequence having a lower abundance of these amino acids relative to BSA and hemoglobin.[72–74] PC2 scores further separated the hemoglobin and collagenous spectra. PC2 loading values for CH_4N^+ and $C_4H_6N^+$ were negatively correlated with the hemoglobin spectral scores, while $C_4H_{10}N^+$, $C_5H_{10}N^+$, $C_5H_{12}N^+$, and $C_5H_8N_3^+$ demonstrated positive correlations; this likewise agrees with the known amino acid compositions for hemoglobin vs. collagen I.[72–74]

Together, the C:N measurements, microscope images, and ToF-SIMS spectral data and PCA support that the permafrost collagen fibers share substantial morphological and chemical similarity with extant analogs. The collagen I framework of these permafrost bones has undergone limited diagenesis relative to the extensive *in-situ* polymerization/carbonization observed for soft tissue specimens of earlier geologic strata.[21–24,77] This agrees with prior studies on bulk permafrost bone extracts that have reported C:N ratios of ∼2.9–3.6, implying relatively minimal alteration of the collagen.[48–50] Likewise, paleoproteomic sequencing studies of permafrost bone generally report sequence coverage for both peptide chains of collagen I (α1 and α2) >50–60%,[42,46,47] roughly comparable to what is reported for extant bone.[51,52] The presence of an observed collagen I framework supports these permafrost bones represent subfossil bone tissue. While extensive alteration of the permafrost collagen was not detected herein, this is unlikely to be the case with specimens from substantially warmer thermal settings and/or earlier geologic strata. Future studies on such specimens can document OBM structural alteration via electron microscopy, as shown by the preliminary data in Figure 1 of Anderson (2022).[30] For ToF-SIMS, indicators of chemical diagenesis would likely include alteration of the intensity and distribution of protein-related ion peaks, as well as an increased presence of secondary ions related to aliphatic and aromatic hydrocarbons and heterocycles.[3,11,78]
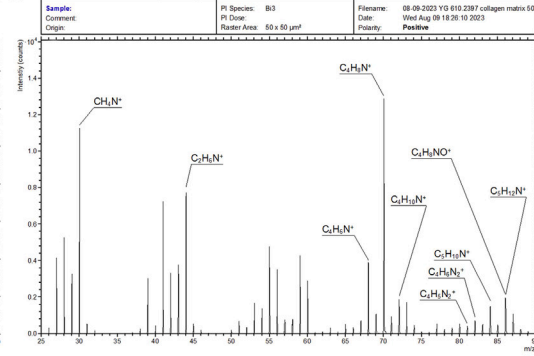
Vascular tissue

"Blood vessels" were isolated/obtained for all specimens by enzymatic digestion of the OBM collagen I framework (Figures 5A1–G1; Figures S2A and S2E). The vessels (interpreted here as representing basal endothelium[79]) were generally clear and flexible and readily
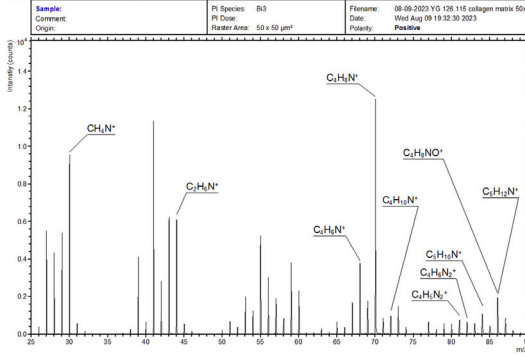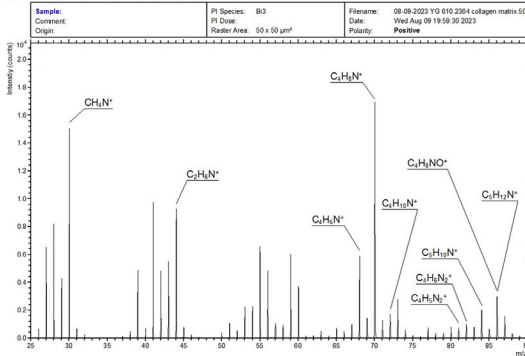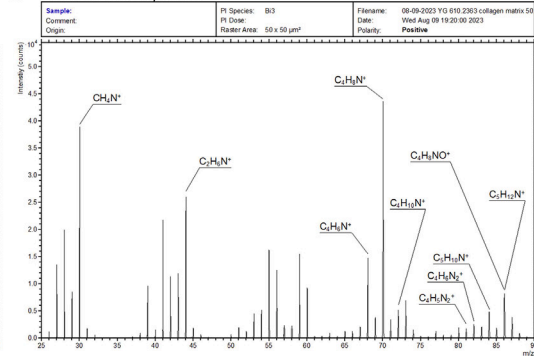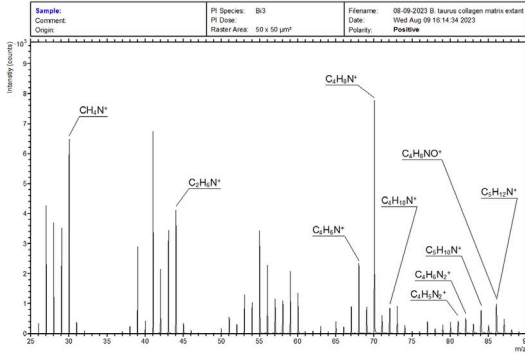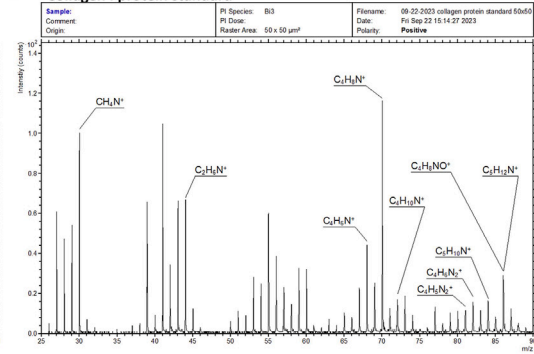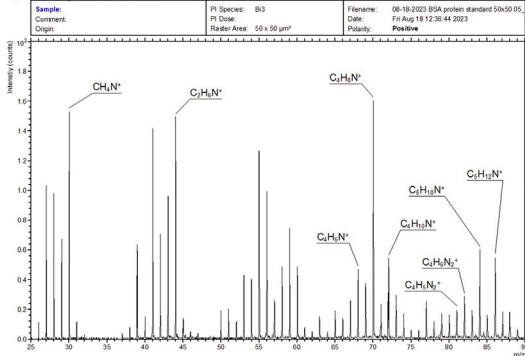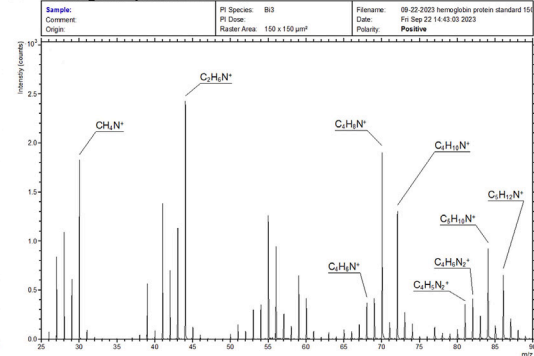
Figure 2. ToF-SIMS spectra of permafrost and extant OBM, and of purified protein standards

Secondary ion peaks for CH_4N^+, $C_2H_6N^+$, $C_4H_6N^+$, $C_4H_8N^+$, $C_4H_{10}N^+$, $C_4H_5N_2^+$, $C_4H_6N_2^+$, $C_5H_{10}N^+$, and $C_5H_{12}N^+$ are labeled for all spectra; the range of each spectrum is limited to 25–90 m/z to aid readability. The ion CH_4N^+ is highly abundant across all the protein-related spectra.[69–71] Both $C_4H_6N^+$ and $C_4H_8N^+$ (proline[69–71]) present as prominent peaks for the collagenous spectra; these peaks are less intense in the hemoglobin standard. At a nominal m/z of 86, substantial peaks for both $C_4H_8NO^+$ (hydroxyproline[75]) and $C_5H_{12}N^+$ (leucine/isoleucine[69–71]) are present for all collagenous spectra (see Figure 3). In contrast, the secondary ion $C_4H_8NO^+$ is not present in the BSA and hemoglobin spectra, thus only $C_5H_{12}N^+$ is labeled. The BSA and hemoglobin spectra also exhibit elevated intensities for $C_4H_{10}N^+$ (valine[69–71]) and $C_5H_{10}N^+$ (leucine/lysine[69–71]) relative to the collagenous spectra.

(A) YG 126.115 OBM spectrum.
(B) YG 610.2397 OBM spectrum.
(C) YG 610.2364 OBM spectrum.
(D) YG 610.2363 OBM spectrum.
(E) Extant *B. taurus* OBM spectrum.
(F) Purified collagen I protein standard (bovine) spectrum.
(G) Purified BSA protein standard spectrum.
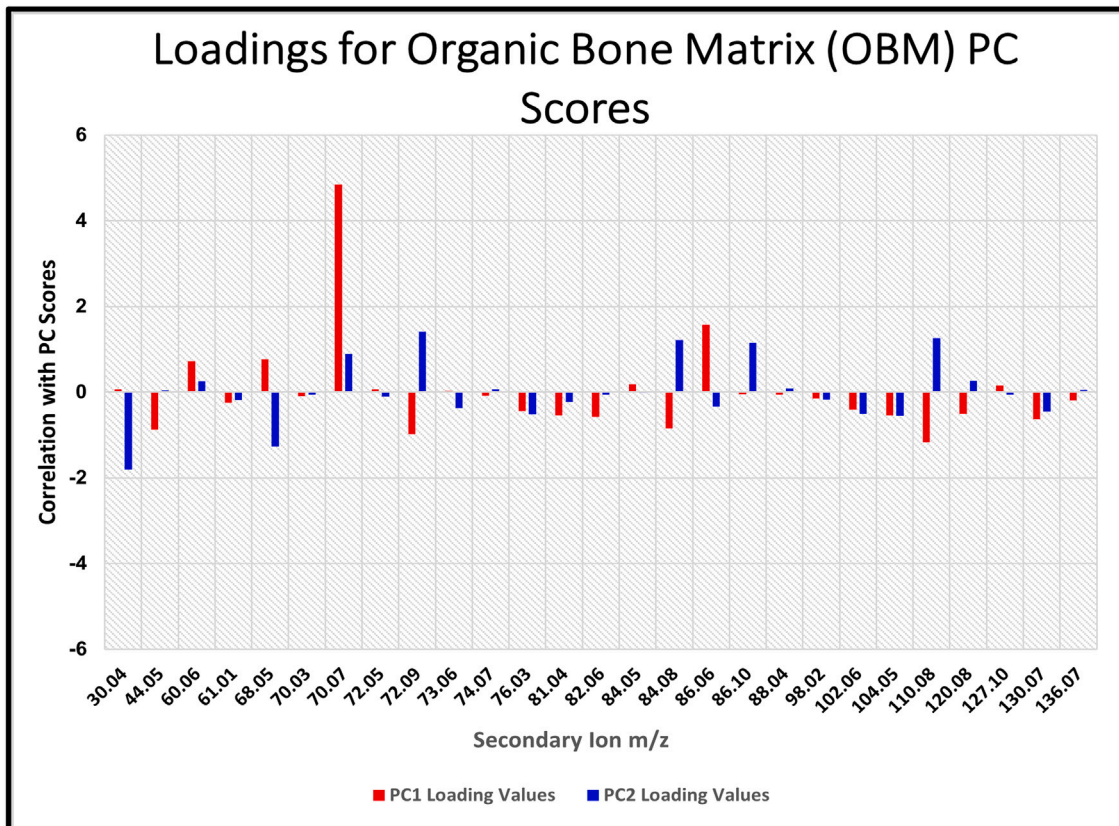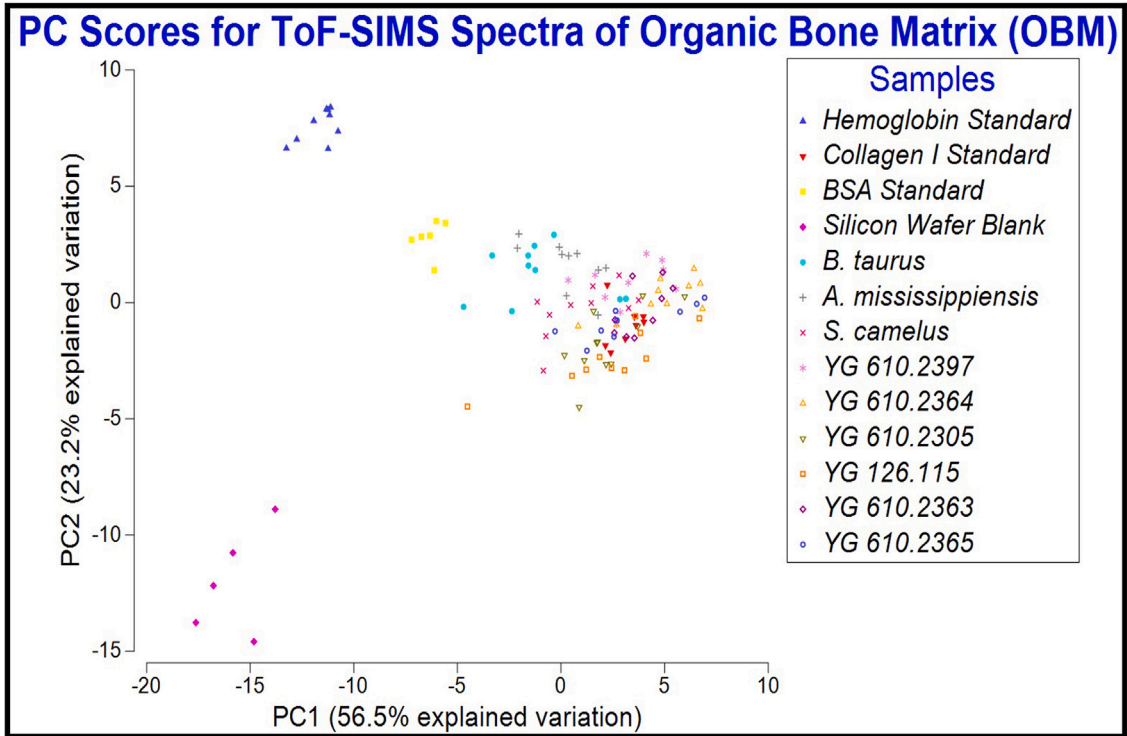(H) Purified hemoglobin (porcine) protein standard spectrum.

sheared in response to excessive turbulence or mechanical force. Some loose, exogenous sedimentary matter was present in portions of the vessel lumens for the permafrost specimens, and fungal hyphae were found to have colonized the vessel lumens of YG 610.2363 and YG 610.2365. Electron microscope imaging revealed a substantial divergence in structure between the permafrost vessels and the extant controls (Figures 5A2–G4; Figures S2B–S2D and S2F–S2H). The vessel "endothelium" of the permafrost specimens consisted of a single, thin "membrane." In contrast, the extant vessel endothelium exhibited more substantial structure, possibly portions of the cytoskeleton as well as cytosolic membranes.[31,80] This disparity suggests that non-collagenous, cellular portions have undergone extensive diagenesis within the permafrost-frozen bones. One exception was YG 126.115 that possessed vessel endothelium somewhat closer in structure to the extant specimens, rather than a single, thin "membrane." Osteocytes (bone cells) were also observed for YG 126.115 as well as for each extant specimen; of the Little Blanche Creek specimens, only YG 610.2364 was observed to harbor osteocytes (Figure S3). Additionally, YG 126.115 possesses soft tissue preserved on the bone's external surface (Figure 1D1). It is the only specimen recovered from the
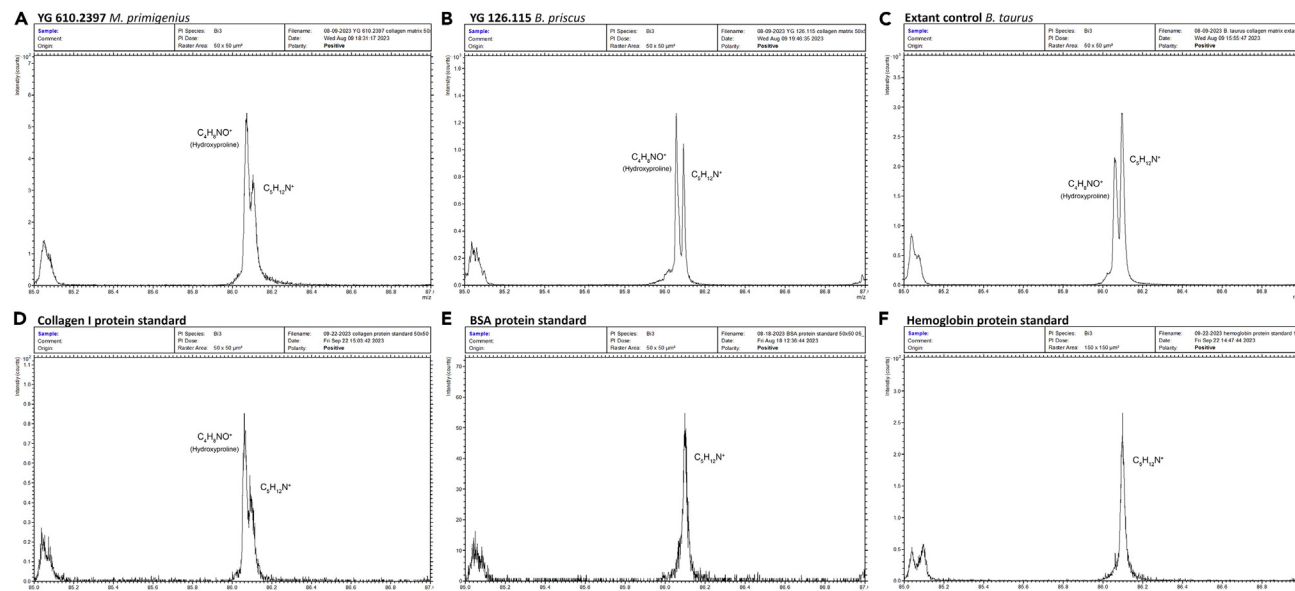
Figure 3. Hydroxyproline-related secondary ion peak for collagenous specimens and protein standards

Enlarged view of secondary ion peaks with a nominal m/z of 86. In SIMS studies of proteinaceous materials, the ion $C_4H_8NO^+$ is primarily formed by fragmentation of hydroxyproline.[75] A peak corresponding to $C_4H_8NO^+$ is present for the OBM spectra (A–C) and the collagen I protein standard (D); such a peak was present for all collagen-related spectra measured (including those not shown in Figure 3). In contrast, this peak is absent in both the BSA and hemoglobin standard spectra (E and F); absence of a substantial peak corresponding to $C_4H_8NO^+$ was observed for all hemoglobin and BSA spectra (including those not shown in Figure 3).

(A) YG 610.2397.
(B) YG 126.115.
(C) Extant *B. taurus*.
(D) Purified collagen I protein standard (bovine).
(E) Purified BSA protein standard.
(F) Purified hemoglobin (porcine) protein standard.

PC Scores for ToF-SIMS Spectra of Organic Bone Matrix (OBM)

Samples
- Hemoglobin Standard
- Collagen I Standard
- BSA Standard
- Silicon Wafer Blank
- B. taurus
- A. mississippiensis
- S. camelus
- YG 610.2397
- YG 610.2364
- YG 610.2305
- YG 126.115
- YG 610.2363
- YG 610.2365

PC2 (23.2% explained variation)

PC1 (56.5% explained variation)

Loadings for Organic Bone Matrix (OBM) PC Scores

Correlation with PC Scores

Secondary Ion m/z

■ PC1 Loading Values ■ PC2 Loading Values

Figure 4. Score and loadings plots for OBM and protein standard ToF-SIMS spectra

Determining the relative abundance of a given secondary ion (and thus amino acid) for a given spectra using PCA requires comparison of score plot values with the loadings plot values. For example, the PC1 loading value for an m/z of 70.07 ($C_4H_8N^+$) is 4.85. This indicates a strong positive correlation for $C_4H_8N^+$ peak intensity with higher PC1 scores. Thus, sample spectra with PC1 scores that are more positive exhibit a greater relative $C_4H_8N^+$ peak intensity. The collagenous spectra exhibited strong positive correlations for PC1 with the ions $C_4H_8N^+$ (70.07 m/z, proline) and $C_4H_8NO^+$ (86.06 m/z, hydroxyproline), and some notable negative correlations with $C_4H_{10}N^+$ (72.09 m/z, valine), $C_4H_5N_2^+$ (81.04 m/z, histidine), $C_4H_6N_2^+$ (82.06 m/z, histidine), $C_5H_{10}N^+$ (84.08 m/z, leucine and lysine), and $C_5H_8N_3^+$ (110.08 m/z, histidine).

Irish Gulch locality (the others being from Little Blanche Creek), suggesting a potential disparity in diagenetic processes between the two sites.

Negative ion ToF-SIMS spectra (Figure 6; Figures S17–S25) were collected for vascular tissue as shown in Figure 5. Protein-related peaks were not studied because the enzymatic digestion used to isolate the vessels introduces a potential source of non-specific peptide signal. In vessels from the extant controls, molecular ions (non-fragmentary secondary ions) corresponding to a variety of fatty acids were present; this was especially the case for palmitic ($C_{16}H_{31}O_2^-$) and oleic ($C_{18}H_{33}O_2^-$) acids.[81] These two fatty acids tend to be the most abundant within extant mammalian tissue including bone.[82,83] Molecular ions for stearic acid, as well as potentially palmitoleic, myristic, margaric, and linoleic acids were also consistently observed; these latter ions, however, may also be attributable to fragment ions of palmitic, oleic, and stearic acids[81] (see Table S2 for a list of secondary ions and their potential source fatty acids). For the Little Blanche Creek permafrost specimens, no secondary ions could be confidently attributed to fatty acids. Secondary ions corresponding to stearic, and particularly palmitic, acids were observed sporadically but generally of limited intensity. The preferential preservation of these fatty acids would be expected in ancient specimens; their lack of hydrocarbon alkene (–CH=CH–) bonds increases chemical stability.[11,84] Previous lipidomic studies have likewise reported the presence of palmitic and stearic acids in ancient remains.[47,85,86] The limited mass resolution of the conventional ToF mass analyzer, however, hinders identification of these "fatty acid" secondary ion peaks for most of the permafrost specimens due to their sporadic nature[87] (see commentary given in Methods S2 of the supplemental information). This was compounded by many of these "peaks" for the ancient specimens expressing low signal relative to instrumental background noise. An exception was YG 126.115, which consistently exhibited ion peaks with similar distributions and intensity to those of the extant control fatty acid secondary ions. This agrees with the morphological disparities documented in Figure 5 and further suggests the cellular components of YG 126.115 have undergone limited chemical diagenesis relative to the Little Blanche Creek specimens.

Figure 7 shows PC1 (70.9% explained variation; PC2 explained 25.5%; see Table S2 for selected peaks) scores for both YG 126.115 and the extant controls were generally negative and clustered together. However, the PC1 scores for these specimens also showed substantial variance and several "outliers" were observed. The loading values for PC1 indicate this was largely due to inconsistency of the palmitic and oleic acid molecular ion signal intensities. Fatty acid composition is known to differ throughout the cellular membranes of eukaryotic organisms[88] and potentially explains this observance. Compounding this, damage to the vessels may have exposed internal cytosolic membranes, exacerbating sample inhomogeneity. Such damage is likely attributable to the method of air-drying the vessels onto silicon wafers; the surface tension of the evaporating water droplet potentially damages the vessel membranes.[89] Regardless, this is one limitation to analyzing structures that are chemically complex, such as cellular membranes, as opposed to the collagen fibers of OBM. In contrast, positive PC1 scores were consistently obtained for the permafrost specimens (minus YG 126.115). The loading value for the peak corresponding to palmitic acid shows a positive correlation with PC1 scores. This suggests that potential fatty acids preserved (if the ions do indeed result from fatty acids, which is itself questionable) within the Little Blanche Creek vascular tissue are enriched with palmitic acid relative to extant specimens. Previous lipidomic studies of ancient mammalian tissues have also consistently reported this phenomenon.[47,85,86,90] A potential explanation may be found in considering the predominance of palmitic and oleic acids within mammalian tissues during life.[82,83] Postmortem, palmitic acid, having a saturated hydrocarbon chain, would preferentially preserve over the unsaturated, more labile oleic acid.[11,84] Stearic acid, the saturated analog of oleic acid, is also favored to preserve; however, initial concentrations of stearic acid in animal tissues tend to be lower relative to both palmitic and oleic acids.[82,83] Thus, palmitic acid may be predicted to be the fatty acid species with the highest preservation potential within diagenetically altered mammalian tissues.

The data support that vascular tissue of the Little Blanche Creek specimens has undergone substantial diagenesis. Vascular structure is reduced to a single, thin "membrane," and secondary ion signal corresponding to fatty acids was detected sporadically (if at all) and with limited intensity. These findings suggest the original lipid bilayers have been disrupted, and much of the original cellular machinery is no longer present. This contrasts sharply with, for example, the frozen cells of one *Mammuthus primigenius* carcass in which the cellular mechanisms for DNA repair were able to be reactivated post-thawing.[54] As a comparison from this study, examined vascular tissue of the YG 126.115 tibia demonstrated secondary ion distributions (for fatty acid m/z values) mirroring those of the extant control spectra; its vessels also presented with somewhat more structure relative to the other permafrost specimens. This suggests that bones preserved in permafrost vary widely regarding degree of cellular preservation. The freezing process largely arrests diagenetic reactions.[91,92] Thus, these taphonomic disparities are likely attributable to events that occurred prior to freezing, or perhaps during a period of thawing. This is supported by the presence of desiccated soft tissue on the external surface of YG 126.115. For such tissue to preserve, relatively rapid freezing likely must have occurred. The Little Blanche Creek bones may have taken longer to be incorporated into permafrost, or local conditions at the Little Blanche Creek site may have promoted diagenesis prior to freezing.[92,93] Such disparities in preservation state for permafrost bones have previously been explored[92,94] but until this study had not been documented at the nanoscale in terms of biomolecular histology.
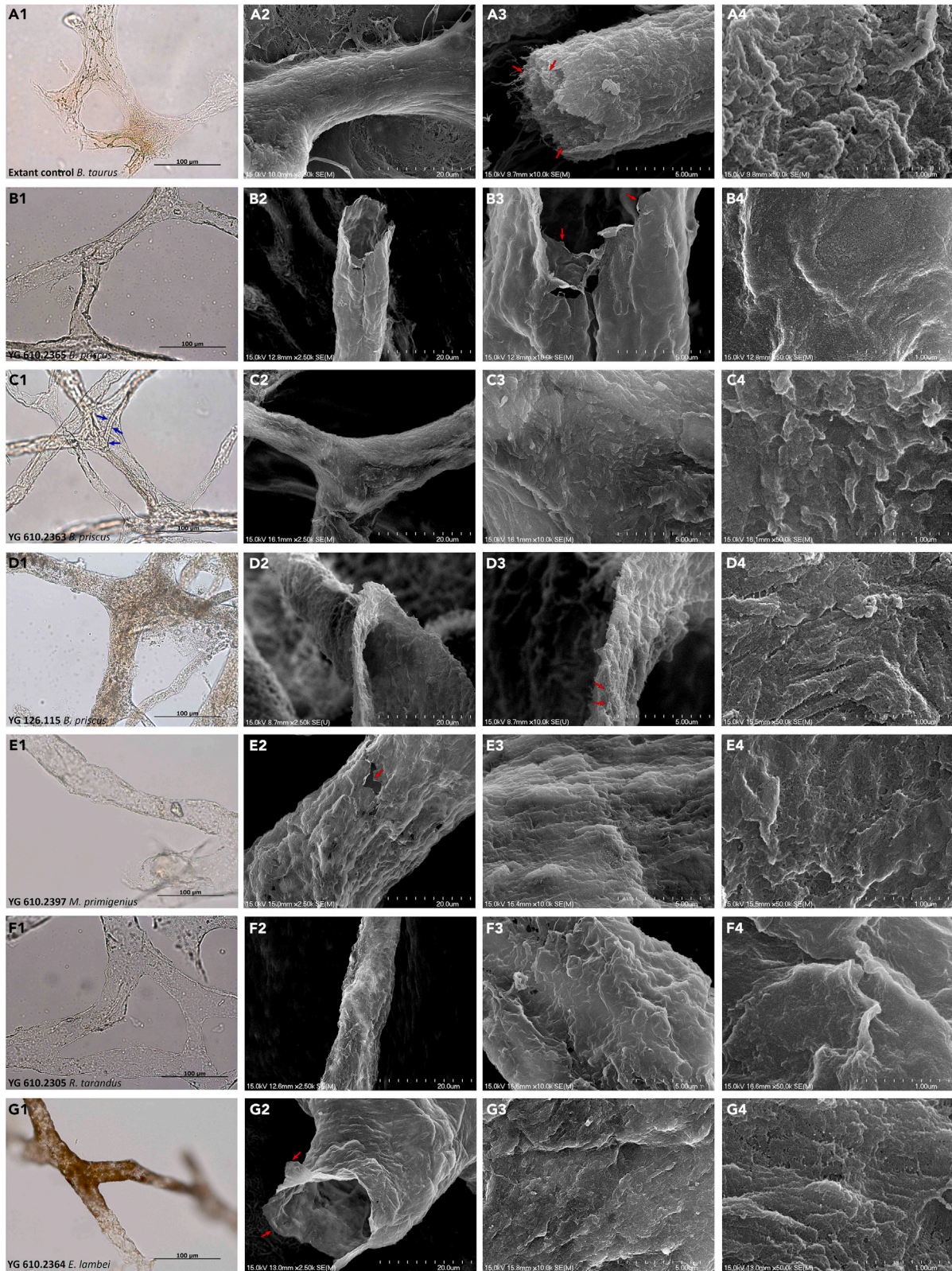
Figure 5. Images of permafrost and extant vascular tissue

(A1–A4) Extant *B. taurus*. The capillary lumen of (A3) reveals the fibrous and membranous structure (denoted by red arrows) of the endothelium.

(B1–B4) YG 610.2365 (*B. priscus* radius). The vessel endothelium (B3) presents as a single, thin "membrane" lacking significant structure (denoted by red arrows). This contrasts with the proteinaceous fibers and membranous portions of the extant *B. taurus* capillary (A3).

(C1–C4) YG 610.2363 (*B. priscus* metatarsal). Images of the vessel lumen are not shown but were comparable to the other Little Blanche Creek specimens. The blue arrows in (C1) denote a fungal hypha.

(D1–D4) YG 126.115 (*B. priscus* tibia). The endothelial membrane (D3) is thin but presents with more structure (denoted by red arrows) relative to the Little Blanche Creek specimens.

(E1–E4) YG 610.2397 (*M. primigenius* innominate). An example of loose sediment in some of the vessel lumens is shown in E1. Additionally, the small tear of the vessel membrane (E2; denoted by red arrow) shows similar morphology with images (B2 and B3).

(F1–F4) YG 610.2305 (*R. tarandus* antler).

(G1–G4) YG 610.2364 (*E. lambei* metatarsal). The vessel "membrane" morphology (denoted by red arrows) in (G2) is comparable to vascular tissue for the other Little Blanche Creek specimens.

Regarding chemical diagenesis, molecular ions for fatty acids were generally absent/attenuated from the Little Blanche Creek vessel spectra, suggesting many of the original biomolecules have undergone chemical alteration. Direct examination of fragmentary organic ions in the lower m/z spectral regions (~20–100 m/z, spectral region not shown) did not reveal any particularly striking differences between the Little Blanche Creek and extant vasculature. Tissues that preserve in pre-Pleistocene strata are known to be highly cross-linked and possess a higher carbon content relative to extant tissues[11,21,95]; however, the C:N ratios and %C and %N measurements reported herein likely rule out extensive carbonization.[11] This is unsurprising given the colder thermal setting and somewhat recent geologic time point. Extensive crosslinking is also likely ruled out as it generally leads to the formation of new molecular structures (such as heterocycles[8,11]) that would alter the secondary fragment ions observed in the lower m/z region. Limited diagenetic crosslinking, such as that observed by Poinar et al. 1998,[96] could be present but is difficult to confirm with the current data. Additionally, as static-SIMS only samples the uppermost ~1–2 nm of specimen surface, a higher degree of biomolecule preservation may be present within the internal portions of the thin vascular "membrane" observed for these specimens. Regardless, the original fatty acids/phospholipids have, to an extent, been altered for the Little Blanche Creek bones, suggesting DNA preservation and protein diversity are also somewhat reduced relative to YG 126.115.

The presented data support YG 126.115 to have a diagenetic history unique from that of the other permafrost specimens and would therefore be preferable for molecular sequencing. Vascular tissue of specimen YG 126.115 did not exhibit the degree of diagenetic alteration observed for the other permafrost specimens. This is a preliminary example of how biomolecular histology may be useful as a proxy for screening specimens for ancient sequencing studies.[30] To truly test this, the permafrost bones of this study would need to undergo a molecular sequencing assay. This would allow cross-comparison of recovered peptide sequences with the data reported herein but is outside the scope of this current study.

Next steps in studying the biomolecular histology of fossil and subfossil bone tissue

Next steps to be taken in expanding upon this present study are 2-fold. Initially, the nanoscopic imaging approach used herein can be readily expanded to Pleistocene bones of warmer (temperate and subtropical) thermal settings as well as specimens from pre-Pleistocene strata. The biochemical preservation of such Cenozoic specimens is not well known and underlying biomolecular histology has only been documented within a few isolated studies.[30,58–60,77] Applying the methods of this present study to a broader range of specimens will inform on the diagenetic changes biomolecular histology undergoes as a function of thermal setting, depositional environment, and/or geologic time point. Secondly, specimens characterized as to their underlying biomolecular histology can additionally be sequenced for ancient DNA and proteins. Correlating biomolecular histological preservation with degree of molecular sequence recovery has potential to establish biomolecular histological analysis as a proxy method for predicting preservation potential for molecular sequences.[30]

As a demonstration of these potential next steps, consider the preliminary data previously reported by Anderson 2022,[30] reproduced within Figures 8A–8C of this current study. Herein, this present study has now extensively documented biomolecular histology for a set of bones directly comparable to those of the preliminary images in Figure 8A (extant *B. taurus* long-bone) and Figure 8B (permafrost-frozen YG 610.2397). The examined extant and permafrost bones (of this present study) each preserve an intact collagen framework, even to the point the original ~67 nm banding pattern is readily observable. Differences in preservation for vascular tissue and osteocytes between YG 126.115 and the Little Blanche Creek specimens potentially suggest YG 126.115 to be the more preferable candidate for sequencing. Overall, however, the permafrost specimens demonstrate relatively good preservation of biomolecular histology, thus exhibiting high preservation potential for sequence-able proteins and potentially DNA.

In contrast, the preliminary image in Figure 8C shows demineralized OBM of the specimen MOR 91.72, a *Mammuthus columbi* femur; this specimen originates from temperate late Pleistocene deposits (Lindsay/Deer Creek) of the state of Montana, United States of America, with an assigned date of ~14–15 Ka (in calibrated years). A collagen framework is observable,[10] but the ~67 nm banding is less distinct, potentially to the point of being absent. This suggests a greater degree of molecular degradation, and such a specimen is likely less ideal for molecular sequencing applications. Indeed, Cappellini et al., 2012,[46] sequenced bones of a permafrost *M. primigenius* specimen (Yakutia, Russia, ~43 Ka) and two temperate *M. columbi* specimens (Colorado, United States, ~11 Ka; Nebraska, United States, ~18 Ka; both states/regions are relatively comparable geographically to Montana). The study reported 1139 unique peptides recovered for the permafrost *M. primigenius*
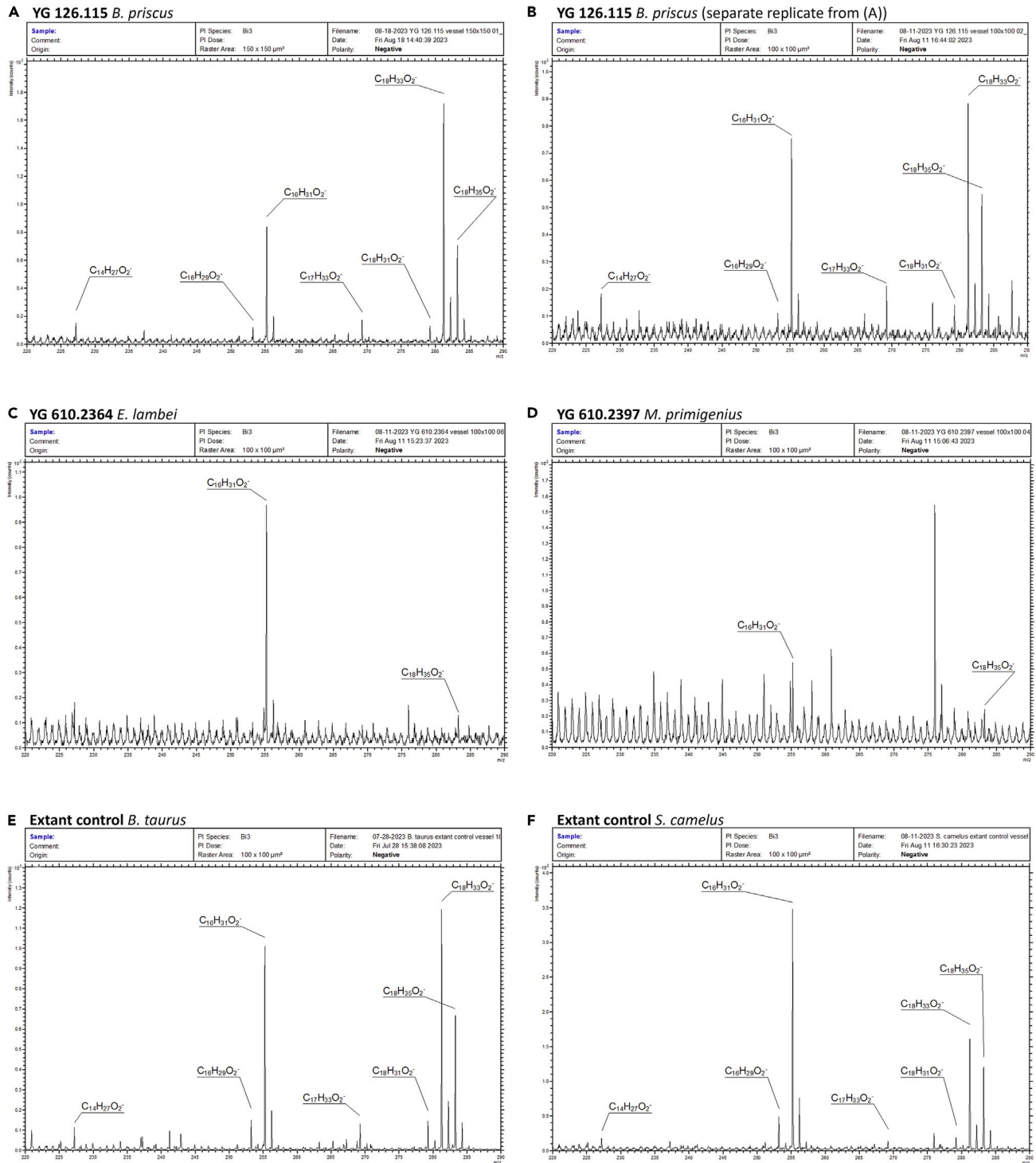
Figure 6. ToF-SIMS spectra of permafrost and extant vascular tissue

Both the YG 126.115 (A and B) and *B. taurus/S. camelus* extant control (E and F) vascular tissue spectra show similar peak distributions for m/z values corresponding to fatty acids. In contrast, the spectra for YG 610.2364 and YG 610.2397 (C and D) show few prominent peaks matching those of the extant controls in (E and F). Additionally, the secondary ion peaks in (C and D) are labeled for clarity only; the labeling is not necessarily an assertion that these secondary ions result from fatty acids. Making such an assertion for these two figured spectra is difficult due to their disparities with the extant controls, and the limited mass resolution of the ToF analyzer (see commentary given in Methods S2 of the supplemental information).

(A) YG 126.115 vascular tissue spectrum.

Figure 6. Continued
(B) YG 126.115 vascular tissue spectrum (separate replicate from (A)).
(C) YG 610.2364 vascular tissue spectrum.
(D) YG 610.2397 vascular tissue spectrum.
(E) Extant *B. taurus* vascular tissue spectrum.
(F) Extant *S. camelus* vascular tissue spectrum.

bone in comparison to 342 and 243 unique peptides recovered for the respective *M. columbi* specimens. This substantial decrease in unique peptide recovery between the permafrost *M. primigenius* bone and the two temperate *M. columbi* bones likewise suggests the temperate MOR 91.72 is a less favorable candidate for molecular sequencing relative to the permafrost bones investigated by this present study.

Figure 8D represents potential analyses of biomolecular histology for bones of even warmer thermal settings and/or earlier geologic strata. Consider the *M. columbi* skull specimen MOR 604, as described within prior studies.[10,30,97] MOR 604 originates from the Doeden gravel beds (also within Montana, United States of America) and shares a relatively comparable thermal setting to MOR 91.72. However, MOR 604 has an assigned date of ~100–600 Ka, and previously published transmitted light microscope data[10,30] has suggested its biomolecular histology is substantially altered relative to MOR 91.72 (as well as the permafrost specimens examined within this present study). Indeed, based on preliminary nanoscopic SEM imaging data (preliminary in the sense that it has not yet been submitted for publication), MOR 604 distinctly lacks a preserved collagen I framework. Despite preservation in the same geographic region and originating from only "slightly" earlier geologic strata, MOR 604 would be considered fossil bone, in contrast to MOR 91.72, which clearly consists of subfossil bone tissue (the underlying, structural collagen framework is preserved). This preliminary finding agrees well with the noticeable drop-off in DNA sequence recovery for temperate specimens of strata prior to the late Pleistocene.[25] The specimen MOR 604 has previously been reported as preserving some remnant collagen I peptides,[97] but, as the relevant study was conducted over two decades ago, the actual degree of molecular sequence preservation is difficult to assess (as regards degree of non-collagenous protein sequence preservation).

Expanding beyond Pleistocene bone specimens, the only pre-Pleistocene bone from which peptide sequences have (thus far) been reported with minimal controversy is an isolated "subfossil" ("subfossil," as termed/defined by the authors of Buckley et al., 2019[98]) camel tibia from the Canadian Yukon territory.[98,99] This prompts the question of how such an exceptional "subfossil" Pliocene bone harboring sequenceable proteins might be differentially preserved relative to the many Pliocene bones lacking such sequences. Particularly, to what degree does this camel tibia preserve intact OBM? Is it preserved similarly to the permafrost bones examined herein by this current study? Is the ~67 nm banding characteristic of collagen fibrils present? Is any biomolecular histology present at all, or are endogenous peptides rather preserved as small, isolated fragments in an otherwise recrystallized, derivative mineral remnant of the original bone? Answers to these questions may be found by using the methods of the present study to evaluate the Pliocene camel tibia's biomolecular histology.

Conclusion

The first extensive nanoscale (up to 150,000× magnification) 3D imaging data of soft tissues for *any* ancient bone are presented in Figures 1 and 5 of this study. The figured data demonstrate the presence of vascular tissue and well-preserved collagen I fibrils within the Pleistocene permafrost bones, indicating the specimens are incompletely fossilized and represent subfossil bone tissue (that is, an underlying collagenous framework is present). Broader application of the methods used herein to bone specimens of warmer thermal settings and earlier geologic strata can elucidate the fine-scale diagenetic changes that biomolecular tissues undergo during fossilization. Such diagenetic changes can be directly imaged (both structurally and chemically) and tracked according to depositional environment, thermal setting, and geologic time point. This would help reveal the fate of biomolecular tissues during fossilization and has potential to serve as a proxy for screening ancient bones for molecular sequence preservation potential.

Limitations of the study

The chemical identification of collagen I protein and lipids using conventional ToF-SIMS is based on a given specimen's overall spectral fingerprint in comparison to the extant controls and/or protein standards. The presence of any one secondary ion peak within a spectrum is generally not sufficient (in-and-of-itself) to confirm the presence of a given amino acid or fatty acid. This is due in part to the somewhat limited mass resolution of conventional ToF mass analyzers.[87] For example, some of the Little Blanche Creek blood vessel spectra show a peak corresponding to palmitic acid (255.24 m/z, $C_{16}H_{31}O_2^-$). In a theoretical sense, there are multiple possible chemical assignments and source molecules for such an m/z value.[81,87] Palmitic acid (or a compound containing palmitic acid, such as a phospholipid) might be considered the most likely source molecule given that the sample is vascular tissue. However, confirming this based on a lone secondary ion peak is difficult, particularly given the ancient nature of these specimens, although fatty acids certainly are known to preserve within permafrost remains.[47,54,85]

Regarding the SEM imaging procedure, the high magnifications (up to 150,000×) and relatively high accelerating voltage (15 kV) used are particularly prone to inducing charge buildup and sample damage. A thin layer (~70–80 Å) of metal (this study used gold-palladium) applied to the specimen surface is generally necessary to help mitigate these issues.[89] Excessive application of metal coating will, however, manifest as a granular texture on the sample surface at higher magnifications (as an example, see Figure 3D of Nix and Feist-Burkhardt[100]). Even with this measure in place, efficient operation of the SEM instrument is essential to avoid excessive irradiation of the sample with the primary electron beam. Additionally, simply air-drying soft tissues for SEM imaging will generally introduce sample damage and artifacts. An alternative
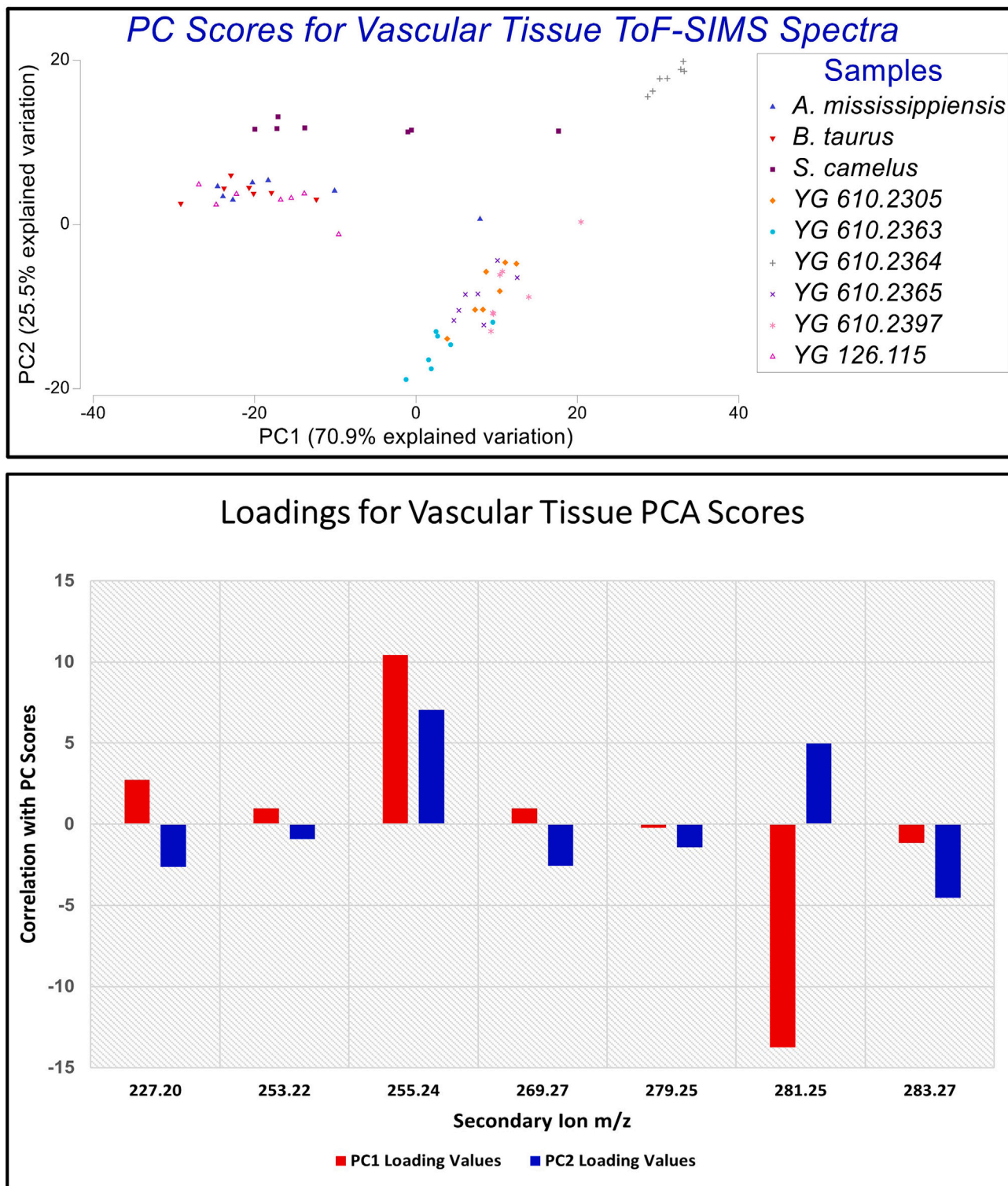
Figure 7. Score and loadings plots for vascular tissue ToF-SIMS spectra

The most predominant molecular ions observed in the extant/YG 126.115 spectra corresponded to palmitic (255.24 m/z) and oleic (281.25 m/z) acids. A majority of the extant/YG 126.115 scores fell within the range −27 to −9, indicating a higher abundance of oleic acid relative to palmitic acid. However, several outliers were observed in the more positive region of the score plot, making it difficult to draw conclusions regarding specific fatty acid prevalence for these specimens. In contrast, the Little Blanche Creek vascular tissue spectra yielded generally higher scores for PC1, indicating a somewhat positive correlation with "palmitic acid" molecular ion abundance (whether the observed peak for the Little Blanche Creek spectra represents palmitic acid, however, is questionable).
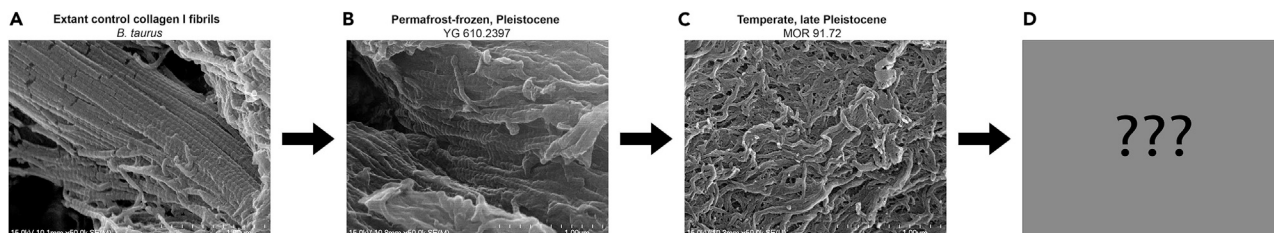
Figure 8. Preliminary SEM images of OBM biomolecular histology reported by Anderson 2022

(A) Extant *B. taurus* long-bone.

(B) Pleistocene, permafrost-frozen YG 610.2397 (*M. primigenius* innominate).

(C) Late Pleistocene, temperate MOR 91.72 (*M. columbi* femur).

(D) Figure 8D represents potential future analyses of biomolecular histology for bones of even warmer thermal settings and/or earlier geologic strata. The images for A–C were originally reported by Anderson (2022)[30] and are reproduced here. Reuse of each of these images by this present study is permitted under the CC BY 4.0 license.

method of sample preparation is generally preferable[89]; in this study, a graded series of ethanol dehydrations followed by critical-point drying was used.

STAR★METHODS

Detailed methods are provided in the online version of this paper and include the following:

- KEY RESOURCES TABLE
- RESOURCE AVAILABILITY
  - ○ Lead contact
  - ○ Materials availability
  - ○ Data and code availability
- METHOD DETAILS
  - ○ Specimens
  - ○ Microscopy
  - ○ Time-of-flight secondary ionization mass spectrometry and principal component analysis
  - ○ Isotopic and C:N measurement

SUPPLEMENTAL INFORMATION

Supplemental information can be found online at https://doi.org/10.1016/j.isci.2024.110538.

AUTHOR CONTRIBUTIONS

Conceptualization, L.A.A.; methodology, L.A.A.; investigation, L.A.A.; writing – original draft, L.A.A.; writing – review & editing, L.A.A.; supervision, L.A.A.

DECLARATION OF INTERESTS

The author declares no competing interests.

REFERENCES

1. Grimaldi, D.A., and Ross, A.J. (2017). Extraordinary Lagerstätten in Amber, with particular reference to the Cretaceous of Burma. In Terrestrial Conservation Lagerstätten: Windows into the Evolution of Life on Land, N.C. Fraser and H.-D. Sues, eds. (Dunedin Academic Press Ltd), pp. 287–342.

2. Brown, C.M., Henderson, D.M., Vinther, J., Fletcher, I., Sistiaga, A., Herrera, J., and Summons, R.E. (2017). An Exceptionally Preserved Three-Dimensional Armored Dinosaur Reveals Insights into Coloration and Cretaceous Predator-Prey Dynamics. Curr. Biol. *27*, 2514–2521.e3.

3. Lindgren, J., Sjövall, P., Thiel, V., Zheng, W., Ito, S., Wakamatsu, K., Hauff, R., Kear, B.P., Engdahl, A., Alwmark, C., et al. (2018). Soft-tissue evidence for homeothermy and crypsis in a Jurassic ichthyosaur. Nature *564*, 359–365.

4. Gupta, N.S., Tetlie, O.E., Briggs, D.E.G., and Pancost, R.D. (2007). The fossilization of eurypterids: A result of molecular transformation. Palaios *22*, 439–447.

5. Stankiewicz, B.A., Briggs, D.E.G., Evershed, R.P., Flannery, M.B., and Wuttke, M. (1997). Preservation of chitin in 25-million-year-old fossils. Science *276*, 1541–1543.

6. Sasso, C.D., and Signore, M. (1998). Exceptional soft-tissue preservation in a theropod dinosaur from Italy. Nature *392*, 383–387.

7. Voegele, K.K., Boles, Z.M., Ullmann, P.V., Schroeter, E.R., Zheng, W., and Lacovara, K.J. (2022). Soft Tissue and Biomolecular Preservation in Vertebrate Fossils from Glauconitic, Shallow Marine Sediments of the Hornerstown Formation, Edelman Fossil Park, New Jersey. Biology *11*, 1161.

8. Wiemann, J., Fabbri, M., Yang, T.-R., Stein, K., Sander, P.M., Norell, M.A., and Briggs, D.E.G. (2018). Fossilization transforms vertebrate hard tissue proteins into N-heterocyclic polymers. Nat. Commun. *9*, 4741.

9. Armitage, M.H., and Anderson, K.L. (2013). Soft sheets of fibrillar bone from a fossil of the supraorbital horn of the dinosaur *Triceratops horridus*. Acta Histochem. *115*, 603–608.

10. Schweitzer, M.H., Wittmeyer, J.L., and Horner, J.R. (2007). Soft tissue and cellular preservation in vertebrate skeletal elements from the Cretaceous to the present. Proc. Biol. Sci. *274*, 183–197.

11. Anderson, L.A. (2023). A chemical framework for the preservation of fossil vertebrate cells and soft tissues. Earth Sci. Rev. *240*, 104367.

12. Senter, P. (2022). Cells and soft tissues in fossil bone: A review of preservation mechanisms, with corrections of misconceptions. Palaeontol. Electronica *25*, a34.

13. Muscente, A.D., Schiffbauer, J.D., Broce, J., Laflamme, M., O'Donnell, K., Boag, T.H., Meyer, M., Hawkins, A.D., Huntley, J.W., McNamara, M., et al. (2017). Exceptionally preserved fossil assemblages through geologic time and space. Gondwana Res. *48*, 164–188.

14. Pfretzschner, H.-U. (2004). Fossilization of Haversian bone in aquatic environments. Comptes Rendus Palevol *3*, 605–616.

15. Keenan, S.W., and Engel, A.S. (2017). Early diagenesis and recrystallization of bone. Geochem. Cosmochim. Acta *196*, 209–223.

16. Keenan, S.W. (2016). From bone to fossil: A review of the diagenesis of bioapatite. Am. Mineral. *101*, 1943–1951.

17. Trueman, C.N., Palmer, M.R., Field, J., Privat, K., Ludgate, N., Chavagnac, V., Eberth, D.A., Cifelli, R., and Rogers, R.R. (2008). Comparing rates of recrystallisation and the potential for preservation of biomolecules from the distribution of trace elements in fossil bones. Comptes Rendus Palevol *7*, 145–158.

18. Collins, M.J., Nielsen–Marsh, C.M., Hiller, J., Smith, C.I., Roberts, J.P., Prigodich, R.V., Wess, T.J., Csapò, J., Millard, A.R., and Turner–Walker, G. (2002). The survival of organic matter in bone: a review. Archaeometry *44*, 383–394.

19. Purnell, M.A., Donoghue, P.J.C., Gabbott, S.E., McNamara, M.E., Murdock, D.J.E., and Sansom, R.S. (2018). Experimental analysis of soft-tissue fossilization: opening the black box. Palaeontology *61*, 317–323.

20. Parry, L.A., Smithwick, F., Nordén, K.K., Saitta, E.T., Lozano-Fernandez, J., Tanner, A.R., Caron, J.-B., Edgecombe, G.D., Briggs, D.E.G., and Vinther, J. (2018). Soft-Bodied Fossils are Not Simply Rotten Carcasses - Toward a Holistic Understanding of Exceptional Fossil Preservation. Bioessays *40*, 1700167.

21. Gupta, N.S. (2014). Biopolymers: A molecular paleontology approach (Springer Science+Business Media Dordrecht).

22. Métais, G., and Sen, S. (2018). The late Miocene mammals from the Konservat-Lagerstätte of Saint-Bauzile (Ardèche, France). Comptes Rendus Palevol *17*, 479–493.

23. Manning, P.L., Edwards, N.P., Bergmann, U., Anné, J., Sellers, W.I., van Veelen, A., Sokaras, D., Egerton, V.M., Alonso-Mori, R., Ignatyev, K., et al. (2019). Pheomelanin pigment remnants mapped in fossils of an extinct mammal. Nat. Commun. *10*, 2250.

24. McNamara, M.E., Orr, P.J., Kearns, S.L., Alcalá, L., Anadón, P., and Peñalver Molla, E. (2009). Soft-Tissue Preservation in Miocene Frogs from Libros, Spain: Insights into the Genesis of Decay Microenvironments. Palaios *24*, 104–117.

25. Dalén, L., Heintzman, P.D., Kapp, J.D., and Shapiro, B. (2023). Deep-time paleogenomics and the limits of DNA survival. Science *382*, 48–53.

26. Buckley, M., Larkin, N., and Collins, M. (2011). Mammoth and Mastodon collagen sequences; survival and utility. Geochim. Cosmochim. Acta *75*, 2007–2016.

27. Wadsworth, C., and Buckley, M. (2014). Proteome degradation in fossils: investigating the longevity of protein survival in ancient bone. Rapid Commun. Mass Spectrom. *28*, 605–615.

28. Demarchi, B., Hall, S., Roncal-Herrero, T., Freeman, C.L., Woolley, J., Crisp, M.K., Wilson, J., Fotakis, A., Fischer, R., Kessler, B.M., et al. (2016). Protein sequences bound to mineral surfaces persist into deep time. Elife *5*, e17092.

29. Boskovic, D.S., Vidal, U.L., Nick, K.E., Esperante, R., Brand, L.R., Wright, K.R., Sandberg, L.B., and Siviero, B.C. (2021). Structural and protein preservation in fossil whale bones from the Pisco Formation (Middle-Upper Miocene), Peru. Palaios *36*, 155–164.

30. Anderson, L.A. (2022). Biomolecular histology as a novel proxy for ancient DNA and protein sequence preservation. Ecol. Evol. *12*, e9518.

31. Alberts, B., Johnson, A., Lewis, J., Raff, M., Roberts, K., and Walter, P. (2002). Molecular Biology of the Cell, 4th edition. (Garland Science).

32. Liu, Y., Luo, D., and Wang, T. (2016). Hierarchical Structures of Bone and Bioinspired Bone Tissue Engineering. Small *12*, 4611–4632.

33. Wegst, U.G.K., Bai, H., Saiz, E., Tomsia, A.P., and Ritchie, R.O. (2015). Bioinspired structural materials. Nat. Mater. *14*, 23–36.

34. Nudelman, F., Pieterse, K., George, A., Bomans, P.H.H., Friedrich, H., Brylka, L.J., Hilbers, P.A.J., de With, G., and Sommerdijk, N.A.J.M. (2010). The role of collagen in bone apatite formation in the

presence of hydroxyapatite nucleation inhibitors. Nat. Mater. *9*, 1004–1009.

35. Cadena, E. (2016). Microscopical and elemental FESEM and Phenom ProX-SEM-EDS analysis of osteocyte- and blood vessel-like structures obtained from fossil vertebrates of the Eocene Messel Pit, Germany. PeerJ *4*, e1618.

36. Cadena, E.A. (2020). In situ SEM/EDS compositional characterization of osteocytes and blood vessels in fossil and extant turtles on untreated bone surfaces; different preservational pathways microns away. PeerJ *8*, e9833.

37. Surmik, D., Boczarowski, A., Balin, K., Dulski, M., Szade, J., Kremer, B., and Pawlicki, R. (2016). Spectroscopic Studies on Organic Matter from Triassic Reptile Bones, Upper Silesia, Poland. PLoS One *11*, e0151143.

38. Schweitzer, M.H., Wittmeyer, J.L., Horner, J.R., and Toporski, J.K. (2005). Soft-Tissue Vessels and Cellular Preservation in *Tyrannosaurus rex*. Science *307*, 1952–1955.

39. Campbell, R.J., and Pignatelli, M. (2002). Molecular histology in the study of solid tumours. Mol. Pathol. *55*, 80–82.

40. Saitta, E.T., Kaye, T.G., and Vinther, J. (2019). Sediment-encased maturation: a novel method for simulating diagenesis in organic fossil preservation. Palaeontology *62*, 135–150.

41. Kohn, M.J. (2008). Models of diffusion-limited uptake of trace elements in fossils and rates of fossilization. Geochem. Cosmochim. Acta *72*, 3758–3770.

42. Orlando, L., Ginolhac, A., Zhang, G., Froese, D., Albrechtsen, A., Stiller, M., Schubert, M., Cappellini, E., Petersen, B., Moltke, I., et al. (2013). Recalibrating *Equus* evolution using the genome sequence of an early Middle Pleistocene horse. Nature *499*, 74–78.

43. Schwarz, C., Debruyne, R., Kuch, M., McNally, E., Schwarcz, H., Aubrey, A.D., Bada, J., and Poinar, H. (2009). New insights from old bones: DNA preservation and degradation in permafrost preserved mammoth remains. Nucleic Acids Res. *37*, 3215–3229.

44. Shapiro, B., Drummond, A.J., Rambaut, A., Wilson, M.C., Matheus, P.E., Sher, A.V., Pybus, O.G., Gilbert, M.T.P., Barnes, I., Binladen, J., et al. (2004). Rise and Fall of the Beringian Steppe Bison. Science *306*, 1561–1565.

45. Mitchell, K.J., and Rawlence, N.J. (2021). Examining Natural History through the Lens of Palaeogenomics. Trends Ecol. Evol. *36*, 258–267.

46. Cappellini, E., Jensen, L.J., Szklarczyk, D., Ginolhac, A., da Fonseca, R.A.R., Stafford, T.W., Jr., Holen, S.R., Collins, M.J., Orlando, L., Willerslev, E., et al. (2012). Proteomic Analysis of a Pleistocene Mammoth Femur Reveals More than One Hundred Ancient Bone Proteins. J. Proteome Res. *11*, 917–926.

47. Kostyukevich, Y., Bugrova, A., Chagovets, V., Brzhozovskiy, A., Indeykina, M., Vanyushkina, A., Zherebker, A., Mitina, A., Kononikhin, A., Popov, I., et al. (2018). Proteomic and lipidomic analysis of mammoth bone by high-resolution tandem mass spectrometry coupled with liquid chromatography. Eur. J. Mass Spectrom. *24*, 411–419.

48. Bocherens, H., Pacaud, G., Lazarev, P.A., and Mariotti, A. (1996). Stable isotope abundances (^{13}C, ^{15}N) in collagen and soft tissues from Pleistocene mammals from Yakutia: Implications for the palaeobiology of the Mammoth Steppe. Palaeogeogr. Palaeoclimatol. Palaeoecol. *126*, 31–44.

49. Metcalfe, J.Z., Longstaffe, F.J., Jass, C.N., Zazula, G.D., and Keddie, G. (2016). Taxonomy, location of origin and health status of proboscideans from Western Canada investigated using stable isotope analysis. J. Quat. Sci. *31*, 126–142.

50. Iacumin, P., Nikolaev, V., and Ramigni, M. (2000). C and N stable isotope measurements on Eurasian fossil mammals, 40 000 to 10 000 years BP: Herbivore physiologies and palaeoenvironmental reconstruction. Palaeogeogr. Palaeoclimatol. Palaeoecol. *163*, 33–47.

51. Buckley, M., Warwood, S., van Dongen, B., Kitchener, A.C., and Manning, P.L. (2017). A fossil protein chimera; difficulties in discriminating dinosaur peptide sequences from modern cross-contamination. Proc. Biol. Sci. *284*, 20170544.

52. Welker, F., Smith, G.M., Hutson, J.M., Kindler, L., Garcia-Moreno, A., Villaluenga, A., Turner, E., and Gaudzinski-Windheuser, S. (2017). Middle Pleistocene protein sequences from the rhinoceros genus *Stephanorhinus* and the phylogeny of extant and extinct Middle/Late Pleistocene Rhinocerotidae. PeerJ *5*, e3033.

53. Glass, J.R., Davis, M., Walsh, T.J., Sargis, E.J., and Caccone, A. (2016). Was Frozen Mammoth or Giant Ground Sloth Served for Dinner at The Explorers Club? PLoS One *11*, e0146825.

54. Yamagata, K., Nagai, K., Miyamoto, H., Anzai, M., Kato, H., Miyamoto, K., Kurosaka, S., Azuma, R., Kolodeznikov, I.I., Protopopov, A.V., et al. (2019). Signs of biological activities of 28,000-year-old mammoth nuclei in mouse oocytes visualized by live-cell imaging. Sci. Rep. *9*, 4050.

55. Boeskorov, G.G., Potapova, O.R., Protopopov, A.V., Plotnikov, V.V., Agenbroad, L.D., Kirikov, K.S., Pavlov, I.S., Shchelchkova, M.V., Belolyubskii, I.N., Tomshin, M.D., et al. (2016). The Yukagir Bison: The exterior morphology of a complete frozen mummy of the extinct steppe bison, *Bison priscus* from the early Holocene of northern Yakutia, Russia. Quat. Int. *406*, 94–110.

56. Serdyuk, N.V., Potapova, O.R., Kharlamova, A.S., Maschenko, E.N., Kirikov, K.S., Pavlov, I.S., Protopopov, A.V., Plotnikov, V.V., Kolesov, S.D., and Klimovskii, A.I. (2016). New data on the internal organs of a frozen Yukagir bison mummy (*Bison priscus* Bojanus, 1827), Yakutia, Russia. Dokl. Biol. Sci. *467*, 89–92.

57. Hattori, S., Kiriyama-Tanaka, T., Kusubata, M., Taga, Y., Ebihara, T., Kumazawa, Y., Imai, K., Miura, M., Mezaki, Y., Tikhonov, A., and Senoo, H. (2021). Preservation of collagen in the soft tissues of frozen mammoths. PLoS One *16*, e0258699.

58. Wyckoff, R.W.G., and Doberenz, A.R. (1965). The electron microscopy of Rancho La Brea bone. Proc. Natl. Acad. Sci. USA *53*, 230–233.

59. Schaedler, J.M., Krook, L., Wootton, J.A.M., Hover, B., Brodsky, B., Naresh, M.D., Gillette, D.D., Madsen, D.B., Horne, R.H., and Minor, R.R. (1992). Studies of Collagen in Bone and Dentin Matrix of a Columbian Mammoth (Late Pleistocene) of Central Utah. Matrix *12*, 297–307.

60. Doberenz, A.R., and Wyckoff, R.W.G. (1967). Fine structure in fossil collagen. Proc. Natl. Acad. Sci. USA *57*, 539–541.

61. Haridy, Y., Osenberg, M., Hilger, A., Manke, I., Davesne, D., and Witzmann, F. (2021). Bone metabolism and evolutionary origin of osteocytes: Novel application of FIB-SEM tomography. Sci. Adv. *7*, eabb9113.

62. Thiel, V., and Sjövall, P. (2011). Using Time-of-Flight Secondary Ion Mass Spectrometry to Study Biomarkers. Annu. Rev. Earth Planet Sci. *39*, 125–156.

63. (2003). 3rd International Mammoth Conference Field Guide to Quaternary Research in the Klondike Goldfields. In Yukon Palaeontology Program, D.G. Froese and G.D. Zazula, eds..

64. Froese, D.G., Zazula, G.D., Westgate, J.A., Preece, S.J., Sanborn, P.T., Reyes, A.V., and Pearce, N.J.G. (2009). The Klondike goldfields and Pleistocene environments of Beringia. GSA Today *19*, 4–10.

65. Sealy, J., Johnson, M., Richards, M., and Nehlich, O. (2014). Comparison of two methods of extracting bone collagen for stable carbon and nitrogen isotope analysis: comparing whole bone demineralization with gelatinization and ultrafiltration. J. Archaeol. Sci. *47*, 64–69.

66. Minary-Jolandan, M., and Yu, M.-F. (2009). Nanomechanical Heterogeneity in the Gap and Overlap Regions of Type I Collagen Fibrils with Implications for Bone Heterogeneity. Biomacromolecules *10*, 2565–2570.

67. Orgel, J.P.R.O., Irving, T.C., Miller, A., and Wess, T.J. (2006). Microfibrillar structure of type I collagen *in situ*. Proc. Natl. Acad. Sci. USA *103*, 9001–9005.

68. Rabotyagova, O.S., Cebe, P., and Kaplan, D.L. (2008). Collagen structural hierarchy and susceptibility to degradation by ultraviolet radiation. Mater. Sci. Eng. C Mater. Biol. Appl. *28*, 1420–1429.

69. Samuel, N.T., Wagner, M.S., Dornfeld, K.D., and Castner, D.G. (2002). Analysis of Poly(amino acids) by Static Time-of-Flight Secondary Ion Mass Spectrometry (TOF-SIMS). Surf. Sci. Spectra *8*, 163–184.

70. Wagner, M.S., McArthur, S.L., Shen, M., Horbett, T.A., and Castner, D.G. (2002). Limits of detection for time of flight secondary ion mass spectrometry (ToF-SIMS) and X-ray photoelectron spectroscopy (XPS): detection of low amounts of adsorbed protein. J. Biomater. Sci. Polym. Ed. *13*, 407–428.

71. Mantus, D.S., Ratner, B.D., Carlson, B.A., and Moulder, J.F. (1993). Static secondary ion mass spectrometry of adsorbed proteins. Anal. Chem. *65*, 1431–1438.

72. Holwerda, A.M., and van Loon, L.J.C. (2022). The impact of collagen protein ingestion on musculoskeletal connective tissue remodeling: a narrative review. Nutr. Rev. *80*, 1497–1514.

73. Zubavichus, Y., Shaporenko, A., Grunze, M., and Zharnikov, M. (2008). Is X-ray Absorption Spectroscopy Sensitive to the Amino Acid Composition of Functional Proteins? J. Phys. Chem. B *112*, 4478–4480.

74. Sanni, O.D., Wagner, M.S., Briggs, D., Castner, D.G., and Vickerman, J.C. (2002). Classification of adsorbed protein static ToF-SIMS spectra by principal component analysis and neural networks. Surf. Interface Anal. *33*, 715–728.

75. Henss, A., Rohnke, M., El Khassawna, T., Govindarajan, P., Schlewitz, G., Heiss, C.,

and Janek, J. (2013). Applicability of ToF-SIMS for monitoring compositional changes in bone in a long-term animal model. J. R. Soc. Interface *10*, 20130332.

76. Miller, E.J., Martin, G.R., Piez, K.A., and Powers, M.J. (1967). Characterization of Chick Bone Collagen and Compositional Changes Associated with Maturation. J. Biol. Chem. *242*, 5481–5489.

77. Matter, P., III, Davidson, F.D., and Wyckoff, R.W.G. (1970). The microstructure and composition of some pliocene fossils. Comp. Biochem. Physiol. *35*, 291–298.

78. Sjövall, P., Bake, K.D., Pomerantz, A.E., Lu, X., Mitra-Kirtley, S., and Mullins, O.C. (2021). Analysis of kerogens and model compounds by time-of-flight secondary ion mass spectrometry (TOF-SIMS). Fuel *286*, 119373.

79. Bergers, G., and Song, S. (2005). The role of pericytes in blood-vessel formation and maintenance. Neuro Oncol. *7*, 452–464.

80. Alberts, B. (1998). The Cell as a Collection of Protein Machines: Preparing the Next Generation of Molecular Biologists. Cell *92*, 291–294.

81. Graham, D.J., Taylor, M.J., Zhang, K.Y., and Gamble, L.J. (2022). Fatty acid and sphingosine reference spectra. Surf. Sci. Spectra *29*, 015001.

82. Steiner-Bogdaszewska, Ż., Tajchman, K., Domaradzki, P., and Florek, M. (2022). Composition and Fatty Acid Profile of Bone Marrow in Farmed Fallow Deer (*Dama dama*) Depending on Diet. Animals. *12*, 941.

83. Bandara, E.M.S., Edirisinghe, D.I.U., Wanniarachchi, D.D.C.d.S., Peiris, H., Perera, P.P.R., Jayakrishan, A.G., Waikar, H.D., Sharma, S.K., Abeysuriya, V., and Chandrasena, L.G. (2022). A comparative study on fatty acid profile in selected vessels of coronary artery bypass graft (CABG). PLoS One *17*, e0260780.

84. Catalá, A. (2010). A synopsis of the process of lipid peroxidation since the discovery of the essential fatty acids. Biochem. Biophys. Res. Commun. *399*, 318–323.

85. Guil-Guerrero, J.L., Tikhonov, A., Rodríguez-García, I., Protopopov, A., Grigoriev, S., and Ramos-Bueno, R.P. (2014). The Fat from Frozen Mammals Reveals Sources of Essential Fatty Acids Suitable for Palaeolithic and Neolithic Humans. PLoS One *9*, e84480.

86. Cersoy, S., Richardin, P., Walter, P., and Brunelle, A. (2012). Cluster TOF-SIMS imaging of human skin remains: analysis of a South-Andean mummy sample. J. Mass Spectrom. *47*, 338–346.

87. Passarelli, M.K., Pirkl, A., Moellers, R., Grinfeld, D., Kollmer, F., Havelund, R., Newman, C.F., Marshall, P.S., Arlinghaus, H., Alexander, M.R., et al. (2017). The 3D OrbiSIMS—label-free metabolic imaging with subcellular lateral resolution and high mass-resolving power. Nat. Methods *14*, 1175–1183.

88. Harayama, T., and Riezman, H. (2018). Understanding the diversity of membrane lipid composition. Nat. Rev. Mol. Cell Biol. *19*, 281–296.

89. Echlin, P. (2009). Handbook of Sample Preparation for Scanning Electron Microscopy and X-Ray Microanalysis (Springer).

90. Mayer, B.X., Reiter, C., and Bereuter, T.L. (1997). Investigation of the triacylglycerol composition of iceman's mummified tissue by high-temperature gas chromatography. J. Chromatogr. B Biomed. Sci. Appl. *692*, 1–6.

91. Jensen, A.M., and Sheehan, G.W. (2014). Frozen Conditions: Preservation and Excavation. In Encyclopedia of Global Archaeology, C. Smith, ed. (Springer).

92. Calábková, G., Chlachula, J., Ivanov, M., Hložková, M., Czerniawska, J., Vašinová-Galiová, M., Prokeš, L., and Gadas, P. (2023). Microbial degradation of Pleistocene permafrost-sealed fossil mammal remains. Quat. Res. *111*, 84–106.

93. Procopio, N., Mein, C.A., Starace, S., Bonicelli, A., and Williams, A. (2021). Bone Diagenesis in Short Timescales: Insights from an Exploratory Proteomic Analysis. Biology *10*, 460.

94. Kuznetsova, T.V., Wetterich, S., Matthes, H., Tumskoy, V.E., and Schirrmeister, L. (2022). Mammoth Fauna Remains From Late Pleistocene Deposits of the Dmitry Laptev Strait South Coast (Northern Yakutia, Russia). Front. Earth Sci. *10*, 757629.

95. Tissot, B.P., and Welte, D.H. (1984). Petroleum Formation and Occurence (Springer-Verlag Berlin Heidelberg).

96. Poinar, H.N., Hofreiter, M., Spaulding, W.G., Martin, P.S., Stankiewicz, B.A., Bland, H., Evershed, R.P., Possnert, G., and Pääbo, S. (1998). Molecular Coproscopy: Dung and Diet of the Extinct Ground Sloth *Nothrotheriops shastensis*. Science *281*, 402–406.

97. Schweitzer, M.H., Hill, C.L., Asara, J.M., Lane, W.S., and Pincus, S.H. (2002). Identification of Immunoreactive Material in Mammoth Fossils. J. Mol. Evol. *55*, 696–705.

98. Buckley, M., Lawless, C., and Rybczynski, N. (2019). Collagen sequence analysis of fossil camels, *Camelops* and c.f. *Paracamelus*, from the Arctic and sub-Arctic of Plio-Pleistocene North America. J. Proteomics *194*, 218–225.

99. Rybczynski, N., Gosse, J.C., Harington, C.R., Wogelius, R.A., Hidy, A.J., and Buckley, M. (2013). Mid-Pliocene warm-period deposits in the High Arctic yield insight into camel evolution. Nat. Commun. *4*, 1550.

100. Nix, T., and Feist-Burkhardt, S. (2003). New methods applied to the microstructure analysis of Messel oil shale: confocal laser scanning microscopy (CLSM) and environmental scanning electron microscopy (ESEM). Geol. Mag. *140*, 469–478.

101. Coplen, T.B., Brand, W.A., Gehre, M., Gröning, M., Meijer, H.A.J., Toman, B., and Verkouteren, R.M. (2006). New Guidelines for δ^{13}C Measurements. Anal. Chem. *78*, 2439–2441.

STAR★METHODS

KEY RESOURCES TABLE

REAGENT or RESOURCE	SOURCE	IDENTIFIER
Biological samples		
Bison priscus tibia	Yukon Government Paleontology Program	YG 126.115
Rangifer tarandus antler	Yukon Government Paleontology Program	YG 610.2305
Bison priscus metatarsal	Yukon Government Paleontology Program	YG 610.2363
Equus lambei metatarsal	Yukon Government Paleontology Program	YG 610.2364
Bison priscus radius	Yukon Government Paleontology Program	YG 610.2365
Mammuthus primigenius innominate fragment	Yukon Government Paleontology Program	YG 610.2397
Chemicals, peptides, and recombinant proteins		
Collagen Type-I (bovine Achilles tendon)	Sigma	CAS: 9007-34-5; Product No.: C-9879
Bovine serum albumin (BSA), heat-shock treated	Fisher	CAS: 9048-46-8; Cat#: BP1600-100
Hemoglobin (porcine)	Sigma	CAS: 9008-02-0; Product No.: H4131-1G
Deposited data		
Raw, unprocessed microscope images	Mendeley Data	doi:10.17632/gnrthwt9j7.1; https://data.mendeley.com/datasets/gnrthwt9j7/1
Collagenous sample ToF-SIMS spectra	Harvard Dataverse	doi:10.7910/DVN/ITLDE7; https://doi.org/10.7910/DVN/ITLDE7
Vascular Tissue ToF-SIMS spectra	Harvard Dataverse	doi:10.7910/DVN/SJ1OX4; https://doi.org/10.7910/DVN/SJ1OX4
Other		
Microporous specimen capsules (30 microns)	Electron Microscopy Sciences	Cat#: 70187-20

RESOURCE AVAILABILITY

Lead contact

Further information and requests regarding resources, reagents, and/or data should be directed to and will be fulfilled by the lead contact, Landon A. Anderson (laander2@ncsu.edu), upon reasonable request.

Materials availability

No new materials or reagents were generated by this study.

Data and code availability

- Raw, unprocessed microscope images have been deposited at the Mendeley Data repository, and ToF-SIMS spectra have been deposited at the Harvard Dataverse repository; the respective datasets are publicly available as of the date of publication. DOIs are listed in the key resources table. Raw data for the stable isotope measurements are available as a part of the published supplemental information.
- This paper does not report original code.
- Any additional information required to reanalyze the data reported in this paper is available from the lead contact upon reasonable request.

METHOD DETAILS

Specimens

Pleistocene bone specimens preserved in permafrost of eastern Beringia were received on loan from the Yukon government via the Yukon Paleontology program. The specimens consisted of 6 isolated, disarticulate bones, as follows: YG 610.2397 (*Mammuthus primigenius*

innominate fragment; Little Blanche Creek, Yukon territory), YG 610.2364 (*Equus lambei* metatarsal; Little Blanche Creek, Yukon territory), YG 610.2305 (*Rangifer tarandus* antler; Little Blanche Creek, Yukon territory), YG 610.2365 (*Bison priscus* radius; Little Blanche Creek, Yukon territory), YG 610.2363 (*Bison priscus* metatarsal; Little Blanche Creek, Yukon territory), YG 126.115 (*Bison priscus* tibia; Irish Gulch, Yukon territory). Specimen YG 126.115 exhibited the preservation of desiccated soft tissue on the external surface of the bone, potentially remnant ligaments, musculature, or tendons.

For the extant control bone specimens, fresh *Bos taurus* long-bones (a humerus and a femur) were obtained from a local butcher immediately post-slaughter of the animals. The animals were not slaughtered for the purpose of this study, and the 2 bones were able to be acquired only because the butcher had no use for them. The bones were immediately placed on ice and stored at $-20°C$ for a period of several months, until they were able to be transported to a lab at North Carolina State University, where they were stored at $-80°C$. The *Struthio camelus* long-bone shaft section is from the same specimen used in Schweitzer et al. (2007)[10] The bone section has been stored under laboratory conditions for the past ~16 years. *Alligator mississippiensis* long-bones were obtained fresh from a local alligator farm and stored at $-20°C$; as with the *Bos taurus* long-bones, these animals were not slaughtered for the purpose of this study. Rather, their bones were obtained as a by-product of the farm's business practice.

Information for the protein standards purchased for the ToF-SIMS analyses are as follows: collagen I protein (Sigma, bovine Achilles tendon, CAS: 9007-34-5, Product No.: C-9879); bovine serum albumin (BSA) (Fisher, heat-shock treated, CAS: 9048-46-8, Cat#: BP1600-100); hemoglobin (Sigma, porcine, CAS: 9008-02-0, Product No.: H4131-1G).

Pleistocene permafrost bone samples were prepared in a dedicated "ancient" clean lab isolated from the extant controls and protein standards, while wearing nitrile gloves, a laboratory coat, a surgical mask, and a bouffant cap. Permafrost specimens were sampled using a hammer and chisel cleaned with 10% bleach followed by 70% ethanol. Preparatory area surfaces for permafrost samples were also sterilized with 10% bleach followed by 70% ethanol. Glassware and consumables were autoclaved prior to use. Solutions for ancient specimens were vacuum filtered (0.220 microns) prior to use in preparation protocols.

Microscopy

Bone fragments (~200–400 mg) were collected from each specimen and incubated in EDTA (0.5 M, pH 8.0) at room temperature for ~1–5 days, until demineralized OBM was achieved. Care was taken to only sample the interior cortical bone that was the least discolored (in the case of the Pleistocene specimens). For light microscopy of demineralized OBM samples, a Zeiss Axioskop 2 plus microscope was used to image specimens mounted on glass slides, and resultant images were saved as "Tiff" files. For SEM imaging of OBM samples, samples were fixed for 1 h on ice in 2.5% glutaraldehyde with washes in phosphate-buffered saline (PBS) before and after fixation. A graded series of ethanol incubations (1 h at 50%, 1 h 70%, 1 h 95%, 3 × 1 h 100% ethanol) was then used to dehydrate the samples. During the series of ethanol incubations, samples were placed within microporous specimen capsules (30 microns, Electron Microscopy Sciences, Cat#: 70187-20). For critical point drying, sputter coating, and imaging, samples were transported from the clean lab to the CHANL core facility at the University of North Carolina at Chapel Hill. Samples were critical point dried (Tousimis Autosamdri-931) and sputter coated (Cressington 108 Auto) with ~80 Å of gold-palladium metal. Imaging was performed with a Hitachi S-4700 Cold Cathode Field Emission Scanning Electron Microscope with the accelerating voltage set to 15.0 kV. Collected images were processed in Adobe Photoshop 2021, using the Levels tool; a histogram stretch, followed by a gamma adjustment, and then a second histogram stretch were applied to each image. The protocol for light microscopy and SEM imaging of bone vasculature was identical to that used for the OBM, except that a collagenase digestion was performed immediately post demineralization to isolate blood vessels from the OBM. This involved thorough washing of the demineralized OBM (ten times in water purified via a Barnstead E-Pure water purification system) to remove EDTA. The matrix sections were then incubated overnight at 37°C in a solution of ~1 mg/mL collagenase (collagenase type I, Worthington Biochemical Corporation, Code: CLSS-1, Cat#: LS004214) dissolved in Dulbecco's PBS (pH 7.2, with 0.1 g/L calcium chloride and 0.1 g/L magnesium chloride added to the standard PBS recipe) with 1% sodium azide (to inhibit potential microbial growth). Isolated vessels were washed in PBS buffer. At this point, either light microscopy or further processing for SEM (starting with glutaraldehyde fixation) was performed, as described for the OBM sections.

Time-of-flight secondary ionization mass spectrometry and principal component analysis

Small bone fragments (~100 mg) were placed in 0.24 M hydrochloric acid to demineralize. After complete demineralization (~1–2 days), OBM sections were removed and washed with E-Pure water. For vascular tissue analysis, the OBM sections were then incubated overnight at 37°C in 1 mg/mL collagenase (collagenase type I, Worthington Biochemical Corporation, Code: CLSS-1, Cat#: LS004214) with 1% sodium azide dissolved in Dulbecco's PBS. Isolated blood vessels were washed twice with E-Pure water. For the collagen I, BSA, and hemoglobin protein standards, chloroform/methanol extraction was necessary to remove residual lipids, despite the "purified" standards having been purchased from companies. A few grams of each standard was incubated for ~30 min with agitation in a 2:1 mixture of chloroform:methanol. The chloroform:methanol solution was then decanted off, and the protein standards washed once with fresh chloroform:methanol solution. The wash solution was decanted off, and the protein standards were left to air dry in a chemical fume hood. Immediately (a few hours before) prior to specimen mounting, silicon wafers (provided courtesy of the Analytical Instrumentation Facility at NC State University) were subjected to an RCA-1 cleaning protocol. The RCA-1 cleaning solution consisted of a heated 5:1:1 mixture of 5 parts E-Pure H_2O, 1 part 25% NH_4OH, and 1 part 30% H_2O_2. Cleaned wafers were washed twice with E-Pure water and left to dry in a laminar flow hood.

For specimen mounting, OBM and blood vessel samples were suspended in sterile E-Pure water and pipetted directly onto the RCA-1 cleaned silicon wafers and allowed to air dry in a laminar flow hood. Protein standards were mounted directly onto copper conducting

tape, provided courtesy of the CHANL core facility at UNC Chapel Hill. The specimens were then immediately transported to the Analytical Instrumentation Facility at North Carolina State University and placed under vacuum within the ToF-SIMS instrument. Sample analysis took place the following day.

A TOF-SIMS V (ION TOF, Inc.) was used to analyze the prepared OBM, blood vessel, and protein standard samples. Analyses were performed with a Bi_3^+ liquid metal ion gun at 45° incident to the sample surface under an ultra-high vacuum of $\sim$7.9 × 10^{-9} mbar. Regions of 50 × 50, 100 × 100, or 150 × 150 μm^2 were scanned using the instrument's high current-bunched (high mass resolution) setting with a beam diameter of $\sim$10 microns, a pulse width of $\sim$1 ns, and a cycle time of 100 μs. Data were recorded in the instrument's positive mode for OBM sections and protein standards, and in the negative mode for vascular tissue. Images obtained were 128 × 128 pixels with 1 shot/pixel/raster at an approximate target current of 0.33 pA (this was checked using a Faraday cup prior to each analysis session to ensure the static "limit" was not exceeded). Primary ion dosage was kept below 10^{12} ions/cm^2 to ensure all analyses were performed under static conditions. Resultant spectra had a mass resolution of $\sim$3,000–6,000 m/Δm, dependent on degree of charging and analysis area topography. An electron flood gun was used for charge compensation to mitigate charging-related issues such as degraded mass resolution and attenuated secondary ion signal. When degraded mass resolution (or even peak splitting) due to sample topography was encountered, relatively flat regions of interest within the analysis area were selected to mitigate this issue.

A Poisson correction was applied to the spectra to correct for missed ion counts during instrument dead time. Positive mode spectra were calibrated using the secondary ions $C_2H_3^+$, $C_3H_5^+$, $C_3H_7^+$, $C_4H_7^+$, and $C_5H_7^+$. Negative mode spectra were calibrated with the secondary ions C_3H^-, C_5H^-, C_6^-, and C_6H^-. Manually selected peak lists of 27 amino acid-related secondary ion fragments (Table S1) and 7 fatty acid-related ions (Table S2) were applied to the positive and negative mode spectra, respectively. The amino acid-related peak list was selected based on Mantus et al. 1993, Samuel et al. 2002, Wagner et al. 2002, and Henss et al. 2013.[69–71,75] Areas for secondary ion peaks within the peak lists were calculated and placed in respective data matrices. Resultant data matrices (one each for the positive and negative mode spectra, respectively) were processed using Primer 7 software (version 7.0.23; Primer-E, Quest Research Lmtd., Auckland, New Zealand). Extracted peak areas were standardized to their respective spectrum's summed intensity for all secondary ions included in the respective peak list. PCA was then performed on each of the 2 standardized data matrices, with resultant PC scores and loadings plotted on separate graphs. Loading values were calculated from the eigenvectors (these contain the loading values scaled to unity) by multiplying each eigenvector element with the square root of the respective PC's eigenvalue.

Isotopic and C:N measurement

Large bone fragments (several grams) were collected from each of the Pleistocene permafrost and extant bone specimens, with care taken to only sample interior cortical bone with minimal discoloration (in the case of the Pleistocene samples). Bone fragments were completely demineralized in $\sim$0.24 M HCl (the individual pieces in the tubes were all easily cut with sterile razor blades prior to freeze-drying) and incubated for 24 h in 0.1 M NaOH (with thorough wash steps in E-Pure water in between). The samples were then frozen at −80°C and lyophilized overnight.

Lyophilized OBM was then shipped to the University of Delaware Environmental Isotope Science Laboratory, where the remaining analysis protocol was performed by the laboratory manager on a fee-for-service basis. Samples and reference materials (provided by the UD Environmental Isotope Science Laboratory) were ground and loaded into standard weight pressed tin capsules (8 × 5 mm; Elemental Microanalysis). The loaded capsules were then elementally and isotopically analyzed using a Thermo Scientific EA IsoLink IRMS System. Sample combustion/ elemental analysis was performed with a Flash 2000 EA equipped with a MAS200R autosampler. The Flash EA (elemental analyzer) was configured with a single reactor combustion/reduction tube at 1000°C, helium flow of 180 mL/min, and a GC (gas chromatograph) oven at 40°C. The Flash EA was connected via a ConFlo IV universal continuous flow interface to a Delta V IRMS (isotope ratio mass spectrometer), which allowed collection of stable isotope $\delta^{13}C$ and $\delta^{15}N$ values from evolved CO_2 and N_2 (from sample combustion in the EA).

The L-glutamic acid reference samples USGS40 and USGS41a were used for instrument calibration, and the glycine reference samples USGS64, USGS65, and USGS66 were analyzed as comparative controls. Two of the extant and three of the Pleistocene samples were analyzed in-duplicate to ensure reproducibility; resultant standard deviations were generally within $\sim$0.2‰. All values measured for $\delta^{13}C$ are reported relative to Vienna PeeDee belemnite (VPDB) on a scale "normalized such that the of $\delta^{13}C$ values of NBS 19 calcium carbonate and L-SVEC lithium carbonate are +1.95‰ and −46.6‰, respectively" (see Coplen et al., 2006[101]). All measured $\delta^{15}N$ values are reported relative to atmospheric nitrogen ($\delta^{15}N$ AIR).